

## THERMAL INSTABILITY AND PHOTOIONIZED X-RAY REFLECTION IN ACCRETION DISKS

SERGEI NAYAKSHIN<sup>1</sup>, DEMOSTHENES KAZANAS AND TIMOTHY R. KALLMAN

Laboratory for High Energy Astrophysics, NASA/Goddard Space Flight Center, Code 661, Greenbelt, MD, 20771

*Draft version March 21, 2018*

### ABSTRACT

We study the illumination of accretion disks in the vicinity of compact objects by an overlying X-ray source. Our approach differs from previous works of the subject in that we relax the simplifying assumption of constant gas density used in these studies; instead we determine the density from hydrostatic balance which is solved simultaneously with the ionization balance and the radiative transfer in a plane-parallel geometry. We calculate the temperature profile of the illuminated layer and the reprocessed X-ray spectra for a range of physical conditions, values of photon index  $\Gamma$  for the illuminating radiation, and the incident and viewing angles.

In accordance with some earlier studies, we find that the self-consistent density determination makes evident the presence of a thermal ionization instability well known in the context of quasar emission line studies. The main effect of this instability is to prevent the illuminated gas from attaining temperatures at which the gas is unstable to thermal perturbations. Thus, in sharp contrast to the constant density calculations that predict a continuous and rather smooth variation of the gas temperature in the illuminated material, we find that the temperature profile consists of several well defined thermally stable layers. Transitions between these stable layers are very sharp and can be treated as discontinuities as far as the reprocessed spectra are concerned. In particular, the uppermost layers of the X-ray illuminated gas are found to be almost completely ionized and at the local Compton temperature ( $\sim 10^7 - 10^8$  K); at larger depths, the gas temperature drops abruptly to form a thin layer with  $T \sim 10^6$  K, while at yet larger depths it decreases sharply to the disk effective temperature. For a given X-ray spectral index, this discontinuous temperature structure is governed by just one parameter,  $A$ , which characterizes the strength of the gravitational force relative to the incident X-ray flux.

We find that most of the Fe  $K\alpha$  line emission and absorption edge are produced in the coolest, deepest layers, while the Fe atoms in the hottest, uppermost layers are generally almost fully ionized, hence making a negligible contribution to reprocessing features in  $\sim 6.4 - 10$  keV energy range. We also find that the Thomson depth of the top hot layers is pivotal in determining the fraction of the X-ray flux which penetrates to the deeper cooler layers, thereby affecting directly the strength of the Fe line, edge and reflection features. Due to the interplay of these effects, for  $\Gamma \lesssim 2$ , the equivalent width (EW) of the Fe features decreases monotonically with the magnitude of the illuminating flux, while the line centroid energy remains at 6.4 keV. We provide a summary of the dependence of the reprocessing features in the X-ray reflected spectra on the gravity parameter  $A$ , the spectral index  $\Gamma$  and other parameters of the problem.

We emphasize that the results of our self-consistent calculations are both quantitatively and qualitatively different from those obtained using the constant density assumption. Therefore, we propose that future X-ray reflection calculations should always utilize hydrostatic balance in order to provide a reliable interpretation of X-ray spectra of AGN and GBHCs.

*Subject headings:* accretion, accretion disks — radiative transfer — line: formation — X-rays: general — radiation mechanisms: non-thermal

### 1. INTRODUCTION

The importance of X-ray reflection off the surface of cold matter in the spectra of accreting compact objects has been recognized for a long time. Basko, Sunyaev & Titarchuk (1974) discussed the reprocessing of X-rays from an accreting neutron star incident on the surface of the adjacent cooler companion, while Guilbert & Rees (1988) considered such reprocessing in “clouds” of cold matter in the vicinity of AGN. Lightman & White (1988) studied similar reprocessing on the surface of a geometrically thin, optically thick accretion disk, placing the problem within the “standard” paradigm for AGN and Galactic Black Hole Candidates (GBHC) which asserts the pres-

ence of such disks illuminated by an overlying hot corona (e.g., Liang & Price 1977; Galeev, Rosner & Vaiana 1979; Haardt, Maraschi & Ghisellini 1994). The consequences of X-ray reprocessing in this specific geometry (arrangement) have been explored in detail theoretically and observationally.

Lightman & White (1988) and White, Lightman & Zdziarski (1988) computed the Green’s function for the angle-averaged reflected spectrum assuming that the illuminated material is cold, non-ionized, and has a fixed gas density. Soon thereafter, a number of authors included the effects of ionization on the structure of the iron lines and the reflected continuum (e.g., George & Fabian 1991;

<sup>1</sup>National Research Council Associate

Turner et al. 1992). Krolik, Madau & Życki(1994) calculated the X-ray reflection and the iron lines from a putative distant obscuring torus, while Magdziarz & Zdziarski (1995) calculated angle-dependent reflection component off cold matter; Poutanen, Nagendra & Svensson (1996) included polarization in their calculations of the reflected spectra off neutral matter and Blackman (1999) enunciated the influence of the possible concave geometry of the disk on the iron line profile.

To date, the most careful (in terms of the ionization physics) calculations of the X-ray reflection component and the iron lines from ionized accretion disks in AGN are probably those of Ross and Fabian (1993), Matt et al. (1993), Życki et al. (1994), and more recently for GBHCs of Ross, Fabian & Brandt (1997) and Ross, Fabian & Young (1999). All these studies made use of a simplifying assumption, namely that the density in the illuminated gas be constant and equal to the disk mid-plane value. The justification for this assumption was the fact that in the simplest version of radiation-dominated Shakura-Sunyaev disks (Shakura & Sunyaev 1973, hereafter SS73, see their §2a), thought to be the case in the majority of the observed sources, the gas density is roughly constant in the vertical direction. Note that the accretion disk is radiation-dominated as long as dimensionless accretion rate,  $\dot{m} \equiv \eta \dot{M} c^2 / L_{\text{Edd}} \equiv L / L_{\text{Edd}}$  ( $L_{\text{Edd}}$  is the Eddington accretion rate,  $L$  is the disk bolometric luminosity,  $\eta = 0.06$  is the radiative efficiency of the standard disk in Newtonian limit), is greater than about  $\sim 5 \times 10^{-3}$ .

Recently, Ross, Fabian & Young (1999) suggested that the vertical density structure may follow a Gaussian law with the vertical coordinate  $z$  ( $\rho(z) = \rho(0) \exp[-(z/z_0)^2]$ , where  $z_0$  is the scale height, and  $\rho(0)$  is the central disk density). They showed that weakness of the observed Fe features in spectra of some GBHCs could be interpreted as a result of high degree of ionization of the exposed gas, as opposed to the cold matter intercepting a smaller fraction of the emitted X-rays thereby preserving the paradigm of a cold disk with an overlying hot corona<sup>2</sup>.

However, a self-consistent approach requires that the gas density be determined from the condition of hydrostatic equilibrium *solved simultaneously* with ionization, energy balance and radiation transfer equations rather than be assumed. As such, the approximation of the constant gas density was made by Shakura & Sunyaev (1973) for disks heated by viscous dissipation and for large optical depths only. Therefore, even though the disks we will be considering may be radiation dominated, the constant density assumption may apply only to their deep “cooler” layers, where the X-ray heating is negligible. On the contrary, in the upper disk layers, this heating exceeds the viscous heating by orders of magnitude (see §3.2), and thus the constant density approximation of SS73 cannot be simply extended to these layers. Further, a self-consistent density determination is especially important because of the existence of a thermal instability that allows (and requires under some conditions!) illuminated adjacent gas regions to have vastly different densities and temperatures but, by necessity, similar pressure (see Krolik, McKee & Tarter 1981 – hereafter KMT; Raymond 1993; Ko & Kallman 1994; Różańska & Czerny 1996, and Różańska 1999). For

example, when the gas pressure in the illuminated atmosphere falls below a fraction of the incident X-ray radiation pressure  $F_x/c$  ( $F_x$  is the incident flux), the gas temperature may jump from low values (of the order  $\sim 10^5$  Kelvin for AGN) to the Compton temperature, which is typically as large as  $\sim 10^7 - 10^8$  K. This large jump in temperature makes it impossible to approximate the gas density by either a constant or Gaussian profile, as we will see below.

In this paper, we present an X-ray reprocessing calculation that matches or exceeds the most detailed previous works in terms of the radiation transfer and ionization balance calculations, but also relaxes the assumption of the constant gas density. We adopt a plane-parallel geometry and gravity law appropriate for the standard geometrically thin SS73 disk, and solve for the gas density via hydrostatic pressure equilibrium, taking into account the pressure force due to the X-radiation as well.

The structure of the paper is as follows: In §2 we present general considerations on how the thermal instability may influence the X-ray reprocessing and review previously known results. In §3 we describe the numerical methods we use to solve the radiation transfer, ionization, energy, and hydrostatic balance equations. Readers not interested in these details may skip the latter section and proceed to §4, where we show several representative tests and compare our results with those obtained with the usual constant density assumption. Radiation-dominated disks are discussed in §5. Complications arising due to possible X-ray driven gas evaporation in the case of accretion disks with magnetic flares are discussed briefly in §6. We summarize our results and give our conclusions in §7. The Appendix contains notes on the importance of the thermal conduction, two-phase cloudy structure and the intrinsic disk viscous dissipation for the given problem.

## 2. THERMAL IONIZATION INSTABILITY AND X-RAY REFLECTION

In order to simplify our treatment we will assume in what follows that the geometry of the X-ray illuminated gas is a plane parallel one, i.e., the vertical  $z$ -coordinate is the only dimension relevant to the problem. The surface of the accretion disk is illuminated by X-rays with a power-law plus exponential roll-over spectrum (the power law index,  $\Gamma = 1.5 - 2.4$ , the cutoff energy is fixed at  $E_{\text{cut}} = 200$  keV). Note that due to the fact that most of this radiation is thermalized in the disk and consequently re-radiated, the ionizing spectrum consists, in the zeroth approximation, of the incident X-ray spectrum plus the reprocessed black-body radiation with an equal amount of flux. The vertical coordinate  $z$  is counted from the disk mid-plane. The optical depth in the reflecting material is measured from the top of the illuminated layer, i.e.,  $\tau(z = z_t) = 0$ , where  $z_t$  is the vertical coordinate of the reflector’s top, to be found in a full self-consistent calculation.

The existence of multiple temperature solutions for an X-ray illuminated gas at a given pressure was shown by Buff & McCray (1974) and then elaborated by KMT. It was noted that some of these solutions are unstable. This instability conforms to the criterion for thermal instability discovered by Field (1965). He argued that a physical system is usually in pressure equilibrium with its surround-

<sup>2</sup>Similar suggestions were made earlier in an unpublished paper by Nayakshin & Melia (1997c), and in Nayakshin (1998a,b).

ings. Thus, any perturbations of the temperature  $T$  and the density  $n$  of the system should occur at a constant pressure. The system is unstable when

$$\left(\frac{\partial \Lambda_{\text{net}}}{\partial T}\right)_P < 0, \quad (1)$$

where  $P$  is the full gas pressure, and the “cooling function,”  $\Lambda_{\text{net}}$ , is the difference between cooling and heating rates per unit volume (divided by the gas density  $n$  squared).

In ionization balance studies, it is convenient to define the “density ionization parameter”  $\xi$ , equal to (e.g., KMT)

$$\xi = \frac{4\pi F_x}{n_H}, \quad (2)$$

where  $n_H$  is the hydrogen density. For situations in which the pressure rather than the gas density is of physical importance one defines the “pressure ionization parameter” as

$$\Xi \equiv \frac{F_x}{cP_{\text{gas}}}, \quad (3)$$

where  $P_{\text{gas}}$  is the full gas pressure due to neutral atoms, ions and electrons (we neglect the trapped line radiation pressure in this paper). KMT showed that the instability criterion (1) is equivalent to

$$\left(\frac{d\Xi}{dT}\right)_{\Lambda_{\text{net}}=0} < 0, \quad (4)$$

where the derivative is taken with the condition  $\Lambda_{\text{net}} = 0$  satisfied, i.e., when the energy and ionization balances are imposed. In this form, the instability can be readily seen when one plots temperature  $T$  versus  $\Xi$ , since the unstable parts of the curve are the ones that have a negative slope.

In Figure (1), we show several illustrative ionization equilibrium curves for the case with the ionizing X-ray flux  $F_x = 10^{16}$  erg sec $^{-1}$  cm $^{-2}$ , photon spectral index  $\Gamma = 1.9$  and an equal amount of the black-body flux with temperature equal to the effective temperature for the given  $F_x$ , i.e.,  $kT = kT_{\text{eff}} \simeq 10$  eV. Since these curves produce a shape somewhat similar to the letter “S”, they are commonly referred to as “S-curves”. The solid curve shown in Figure (1) was computed assuming that all resonant lines are optically thin, and we will concentrate on this case for now (significance of the other curves in Fig. 1 will be explained in §3.6). One can see that equilibria in temperature range  $kT \sim 20 - 90$  eV and  $kT \sim 150 - 10^3$  eV are unstable. It is also worthwhile pointing out that the instability criterion (eq. [4]) can be shown to be equivalent to  $c_s^2 = dP_{\text{gas}}/d\rho < 0$ , where  $\rho$  is the gas density and  $c_s$  is the sound speed (see Nayakshin 1998c, §4.5.) An imaginary value of the sound speed in the regions with the negative slope of the ionization balance curve is clearly an “unusual” situation, a fact that perhaps helps to clarify the existence of the thermal instability.

A number of authors have investigated the structure of X-ray illuminated atmospheres in the case of a star in a binary system (e.g., Alme & Wilson 1974; Basko et al. 1974; McCray & Hatchett 1975; Basko et al. 1977; London, McCray, & Auer 1981). These authors concluded

that, as one moves from the star’s interior to the atmosphere (that is from  $\Xi \ll 1$  to  $\Xi = \infty$ ), the gas temperature first follows the S-curve until point (a) [cf. Fig. 1] is reached. For  $\Xi > \Xi(a)$ , the photo-ionization heating exceeds the cooling and no equilibrium is possible until the gas heats up to a fraction of the Compton temperature,  $kT_c \gtrsim 1$  keV, where even the high- $Z$  elements become nearly completely ionized. At this state, the gas cooling and heating is effected predominantly by Compton heating and Compton and bremsstrahlung cooling (KMT). The transition from point (a) to point (b) is very sharp<sup>3</sup>. In fact, since in the case of a star the escape energy for a proton is around  $E_{cs} \sim 100$  eV, and the Compton temperature  $kT_c \sim \text{few keV} \gg E_{cs}$ , a strong wind results. McCray & Hatchett (1975) treated the temperature discontinuity as a deflagration wave, in which case the gas pressure is also discontinuous across the (a-b) boundary; it is the momentum flux that is continuous across the transition.

We are primarily interested in the inner part of an accretion disk, where most of the X-rays are produced and where most of the X-ray reprocessing features presumably arise. Because the gas Compton temperature,  $T_c \lesssim 10^8$  K, is smaller than the virial temperature in the inner disk by several orders of magnitude, no thermally driven wind will escape from the system, and thus there should be a static configuration for the X-ray heated layer in this region (see Begelman, McKee & Shields 1983). Thus, the problem of finding the gas density is reduced to finding its hydrostatic equilibrium configuration.

Raymond (1993) and Ko & Kallman (1994) have calculated the structure of the accretion disk atmospheres around LMXBs at large radii with special attention to the unknown origin of the UV and soft X-ray emission lines. The illuminating spectrum was assumed to be thermal bremsstrahlung with  $T = 10^8$  K. The work of these authors was pioneering in that they calculated the density of the illuminated gas using hydrostatic balance, thus taking the thermal instability into account consistently. Rózańska & Czerny (1996), Rózańska (1999) considered the structure of X-ray illuminated disk atmospheres in AGN, including the effects of thermal conduction. The radiation transfer methods used by these last authors did not allow them to study the effects of spectral reprocessing in detail.

Our paper is a natural extension of the work of these authors. Since we study accretion disks in Seyfert 1 Galaxies and GBHCs rather than in LMXBs as did Raymond (1993) and Ko & Kallman (1994), we use the ionizing spectrum typical for Seyfert 1 Galaxies and GBHCs and deal with the innermost part of the accretion disk. Compared with work of Rózańska & Czerny (1996) and Rózańska (1999), we solve the radiation transfer “exactly” by using the exact frequency dependent cross sections and the variable Eddington factor method to take into account anisotropy of the radiation field.

### 3. THE NUMERICAL APPROACH

#### 3.1. Radiation Transfer

Here we describe the part of our code that performs the radiation transfer. The incident X-rays come with a given specific intensity  $I_x(E, \mu)$ , where  $E$  is the photon energy and  $\mu$  is the cosine of the angle that the given direction

<sup>3</sup>The line cooling complicates this situation; we will come back to this question in §3.6

makes with the normal to the surface of the disk (note that  $I_x(E, \mu)$  is the intensity already integrated over the azimuthal angle, i.e., it is  $2\pi$  times the usual radiation intensity). The X-ray intensity is normalized in such a way as to give the total X-ray flux incident on the reflector,  $F_x$  (erg cm<sup>-2</sup> sec<sup>-1</sup>), integrated over all photon energies and all incident angles:

$$F_x = \int_{-1}^0 |\mu| d\mu \int_0^\infty dE I_x(E, \mu). \quad (5)$$

We limit ourselves to treating only  $\tau_{\max} = 4$  upper Thomson depths of the illuminated layers, since it is both sufficient and practical (see §3.2). We break the reflecting layer into  $N_z$  (typically a few hundred) individual bins. The binning is the finest around the discontinuity in the gas temperature and density.

The ultimate goal of the radiation transfer is to find the photon intensity,  $I(E, \mu, \tau_t)$  as a function of photon energy  $E$ , angle (or  $\mu$ ) and position (equivalently  $\tau_t$ ) everywhere in the slab. Luckily, the ionization balance part of the calculations only depends on the intensity integrated over all angles,  $J(E, \tau_t)$ :

$$J(E, \tau_t) = \int_{-1}^{+1} d\mu I(E, \mu, \tau_t), \quad (6)$$

which then allows us to use the variable Eddington factors method (see Mihalas 1978, §6.3). The variable Eddington factors  $g(E, \tau_t)$  are defined as the ratio of the second to the zeroth moment of the photon intensity:  $g(E, \tau_t) \equiv K(E, \tau_t)/J(E, \tau_t)$ , where  $K(E, \tau_t)$  is given by an equation analogous to Equation (6), but with the additional factor of  $\mu^2$  in the integral. Mihalas (1978) shows that the transfer equation then reduces to

$$\frac{\partial^2}{\partial \tau^2} [g(E, \tau_t) J(E, \tau_t)] = J - S, \quad (7)$$

where  $S(E, \tau_t)$  is the source function, defined as

$$S(E, \tau_t) \equiv \frac{\alpha_s}{\alpha_s + \alpha_a} CJ(E, \tau_t) + \frac{1}{\alpha_s + \alpha_a} j(E, \tau_t), \quad (8)$$

where  $\alpha_s$  and  $\alpha_a$  are the scattering and absorption coefficients, respectively:  $\alpha_s = n_e \sigma_{\text{kn}}(E)$ , where  $n_e = 1.2n_H$  is the electron density,  $\sigma_{\text{kn}}(E)$  is the Klein-Nishina cross section;  $\alpha_a = n_H \sigma_a(E)$ , where  $n_H$  is the hydrogen density and  $\sigma_a(E)$  is the continuum absorption cross section calculated by XSTAR (Kallman & McCray 1982; Kallman & Krolik 1986). Further,  $d\tau$  in Equation (7) is a differential of the total optical depth, so that it is a function of both photon energy and the location in the slab ( $\tau_t$ ) and is given by  $d\tau = (\alpha_s + \alpha_a)dz$  where  $dz$  is the extent of the given bin in the  $z$ -direction. Finally,  $j(E, \tau_t)$  is the local gas emissivity integrated over all angles, and  $C$  is the Compton scattering operator, discussed below.

The Compton scattering is treated similarly to the Ross & Fabian (1993) treatment of Compton down-scattering of incident X-rays: the scattered photons are assumed to be distributed according to a Gaussian profile,  $P(E_0 \rightarrow E)$  (normalized to unity), centered at

$$E_c = E_0 (1 + 4\theta - \varepsilon_0), \quad (9)$$

where  $\theta \equiv kT/m_e c^2$  is the dimensionless electron temperature,  $E_0$  is the initial photon energy and  $\varepsilon_0 \equiv E_0/m_e c^2$ . The energy dispersion of the Gaussian is

$$\sigma = \varepsilon_0 (2\theta + (2/5)\varepsilon_0^2)^{1/2} \quad (10)$$

As shown by Ross & Fabian (1993), and as we found in the course of our numerical experimentation, this treatment describes adequately the down-scattering of photons of energy less than  $\sim 200$  keV.

Ross & Fabian (1993) used a modified Kompaneets equation to describe Compton scattering of the low energy photons. We will see in §3.3 that an accurate numerical flux conservation throughout the reflecting layer is a necessary condition for solving the pressure balance satisfactorily. For best numerical flux conservation, we found that it is preferable to treat all the photons in the same way, avoiding division of the photon intensity on the incident and the ‘diffuse’ components. Therefore, we use the same approach (i.e., the Gaussian emission profile) for Compton scattering of photons of all energies. This is permissible, since for most of our applications below, the average photon with  $E \ll m_e c^2$  gains or loses little energy ( $|\Delta E|/E \sim 4\tau_t^2 \theta \ll 1$ ) before it escapes from the layer, and thus Compton scattering is essentially monochromatic. We conducted several tests of Comptonization of different photon spectra by slabs of different temperatures (in the range  $T = 10^5 - 10^8$  K, the typical values for our problem) via both techniques (i.e., the Gaussian emission profile and the Kompaneets equation) and found no noticeable differences in the results for the slabs of Thomson depth  $\tau_t \sim$  few (but see the end of §7). Accordingly, the result of the Compton scattering operator acting on  $J(E, \tau_t)$  in our approach is

$$CJ(E, \tau_t) \equiv -J(E, \tau_t) + J'(E, \tau_t), \quad (11)$$

where  $J'(E, \tau_t)$  is the intensity of once scattered photons found by convolving the Gaussian re-distribution profile  $P(E' \rightarrow E)$  with the unscattered intensity  $J(E, \tau_t)$ :

$$J'(E, \tau_t) \equiv \frac{1}{\sigma_{\text{kn}}(E)} \int dE' J(E', \tau_t) P(E' \rightarrow E) \sigma_{\text{kn}}(E'), \quad (12)$$

The radiation transfer Equation (7) is supplemented by boundary conditions. On the top of the illuminated layer (i.e., for  $\tau_t = 0$ ), we require that the down propagating flux is equal to the incident X-ray flux:

$$h(E, 0)J(E, 0) - \frac{\partial}{\partial \tau} [g(E, 0)J(E, 0)] = F_x(E), \quad (13)$$

where  $h(E, 0)$  is the ratio of the first to the zeroth moment of the intensity at  $\tau_t = 0$  (see Mihalas 1978, §6.3, especially text after Equation (6-42)).

We assume that all of the incident X-ray flux is reprocessed into the thermal disk flux deep inside the disk (e.g., Sincell & Krolik 1997), and that there is also an intrinsic disk flux  $F_d$  whose magnitude is simply given by the formulae of SS73. We found that the most physical and numerically accurate boundary condition is a mirror boundary condition for  $J(E, \tau_{\max})$ , similar to that used by Alme &

Wilson (1974), with the appropriate correction due to the additional disk flux  $F_d$ :

$$\frac{\partial}{\partial \tau} [g(E, \tau_{\max})J(E, \tau_{\max})] = F_d(E). \quad (14)$$

If  $F_d(E) = 0$ , then equation 14 leads to the exact mirror boundary condition, i.e., every photon is reflected without any change in its energy. This is somewhat unphysical because in reality, due to photo-absorption, X-ray albedo is less than unity, but since only a tiny fraction of X-rays will reach the bottom of the reprocessing layer, we are committing a small error.

The variable Eddington factors are obtained in the usual way (Mihalas 1978, §6.3). One defines the function  $u(E, \mu, \tau_t)$  as  $u(E, \mu, \tau_t) \equiv [I(E, \mu, \tau_t) + I(E, -\mu, \tau_t)]/2$  for  $\mu > 0$ . The angle dependent equation of the radiation transfer can then be written as

$$\mu^2 \frac{\partial^2}{\partial \tau^2} u(E, \mu, \tau_t) = J - S, \quad (15)$$

and it can be solved *exactly* once  $J(E, \tau_t)$  and the source function,  $S(E, \tau_t)$ , are known. The solution of this equation allows us to refine our initial estimate for the variable Eddington factors  $g(E, \tau_t)$  and the flux factors  $h(E, \tau_t)$ . These new functions are then employed in Equation (7) to obtain the next iteration of  $J(E, \tau_t)$ . We repeat this cycle without calling XSTAR (i.e., with fixed opacities and emissivities obtained from the last XSTAR call) typically 30 times such that the Eddington factors converge to a good degree.

### 3.2. Photoionization Calculations

Our treatment of the thermal and ionization balance is closest to the work of Życkiet al. (1994). As mentioned earlier, we use the photoionization code XSTAR (Kallman & McCray 1982; Kallman & Krolik 1986). We start from the first zone situated on the top of the reflecting gas and work our way to the bottom of the layer. We provide XSTAR with the ionizing intensity,  $J(E, \tau_t)$ , for each zone computed in the previous iterations or given by the initial value for the first iteration. The resonance line optical depth for photons emitted in the first layer is assumed to be zero for each line included in XSTAR. The latter then provides us with line opacities for this zone, which we use to compute the line optical depths for the line photons emitted in the next zone. We repeat this process for every spatial bin; therefore, the optical depth of a particular resonant line is a sum of the appropriate line depths for all the previous zones above the given one.

The treatment of the coldest part of the reflecting layer deserves special attention. In terms of the number of the included elements, ionization states and excited states XSTAR is one of the most extensive codes existing at the present time. However, the code does not include stimulated emission or de-excitation processes of certain excited states, so it may incorrectly estimate the cooling rate under some conditions. As in Raymond (1993) and Życkiet al. (1994), we set the gas temperature to the effective one ( $T_{\text{eff}}$ ), if the value computed by XSTAR is lower than  $T_{\text{eff}}$ . Clearly, this approximation is not very accurate for photon energy  $\sim \text{few} \times kT_{\text{eff}}$ , and may not give correct opacities

and emissivities in that energy range. The focus of this paper, however, is on the X-ray reflection feature and the iron line, i.e. the photon energy range  $E \gtrsim 1$  keV, so that the approximation described above should suffice.

Further, in most previous studies, one usually sets a constant black-body or modified black-body continuum to propagate in the upward direction (e.g., Ross & Fabian 1993; Ko & Kallman 1994; Życkiet al. 1994). Since we intend to include the radiation pressure in the hydrostatic balance equation, this approach is not suitable for us. We need to propagate the quasi-thermal component through the layer just as we do the X-rays. The difficulty with this is that we previously introduced the minimum temperature  $T = T_{\text{eff}}$ , which forbids XSTAR to solve the energy balance equation if it leads to  $T < T_{\text{eff}}$ . Therefore, the opacities and emissivities obtained from XSTAR in this way will not match each other (i.e., total energy absorbed  $\neq$  total energy emitted). To cope with this problem, we redefine the emissivities obtained from XSTAR in this regime in the following manner: when  $T = T_{\text{eff}}$ , we count the line emission only if the line energy  $E > 100$  eV, otherwise we set it to zero (because we are mostly interested in the X-ray emission). The continuum emission is assumed to be given by  $j(E, \tau_t) = \alpha_a B(E, T_{\text{eff}})$ , where  $B(E, T_{\text{eff}})$  is the Planck function at  $T = T_{\text{eff}}$ . This choice of  $j(E, \tau_t)$  is appropriate since it is exactly the Kirchoff-Planck law and is often adopted as an expression for the rate of thermal emission. The quasi-thermal emission spectrum  $j(E, \tau_t)$  is renormalized in such a way as to satisfy the energy equilibrium equation.

Finally, one practically important question is how deep in the illuminating layer should we carry our calculations (i.e., how large should  $\tau_{\max}$  be?). In terms of the energy balance for the illuminated layer, it is sensible to extend the computational domain down to the Thomson “viscous heating depth”,  $\tau_{vh}$ , such that for  $\tau_t > \tau_{vh}$  the intrinsic disk viscous heating wins over the X-ray heating. To estimate value of  $\tau_{vh}$ , we proceed in the following manner. The intrinsic disk heating per hydrogen atom, in the framework of SS73 model, is  $Q_d^+ = F_d/(n_H(0)H)$ , where  $n_H(0)$  is the mid-plane hydrogen density. Further, we follow Sincell & Krolik (1997), who derived a useful approximate expression for the X-ray heating rate (see their equation 32). Re-writing it in terms of Thomson depth in the limit  $\tau_t \gg 1$ ,

$$Q_x^+ \sim 0.33 \sigma_t F_x \left[ \frac{\exp(-\tau_t/22)}{\tau_t} \right]. \quad (16)$$

Hence, the ratio of the X-ray heating rate to viscous dissipation is

$$\frac{Q_x^+}{Q_d^+} \sim 0.33 \frac{F_x}{F_d} \frac{\tau_d}{\tau_t} \exp(-\tau_t/22), \quad (17)$$

where  $\tau_d$  is the total Thomson depth of the accretion disk. Clearly, the X-ray heating exceeds the viscous heating by orders of magnitude for  $\tau_t \lesssim 20$ , unless  $F_x \ll F_d$ , a situation of no particular interest to us. Accordingly, we neglect the viscous heating in the illuminated layer (although see the Appendix).

Further, it is computationally impractical to extend computational domain to  $\tau_t \sim 20$ , since the computing

resources are limited. Fortunately, very few X-rays penetrate to Thomson depth greater than  $\tau_t \gtrsim$  few. Therefore, we choose to treat with the full formalism developed in this paper only the upper 4 Thomson depths. In addition, in order to reproduce the thermal component in the reflected spectra, one ought to have some material at that temperature (since our mirror boundary condition does not by itself create thermal flux in the limit  $F_x \gg F_d$ ). In the realistic situation, this material lies below  $\tau_{vh} \gtrsim 20$ , according to the foregoing discussion. Since we limit ourselves to  $\tau_{\max} = 4$ , we instead require that the gas temperature always be the effective temperature for  $3 < \tau_t \leq 4$ . Via numerical experimentation, we found that the Thomson depth of  $\tau_t = 3$  is indeed adequate to compute the reprocessing features, and that the region  $3 < \tau_t \leq 4$  is sufficiently optically thick to produce the thermalized part of the reflected spectrum even if  $F_d = 0$ . These restriction on  $\tau_t$  does not affect our results at all. As we found (see fig. 4) our highest ionization case becomes “cold” below  $\tau_t \simeq 2$ . As apparent in fig. (6) in this specific case the associated reprocessing features are extremely weak. Therefore, in a situation in which the ionized layer extends to  $\tau_t > 3$  such features would be completely unobservable.

### 3.3. Hydrostatic balance

Currently, one of the most widely considered models of the X-ray emission from accretion disks is that where X-rays come from localized active regions, thought to be magnetic flares (e.g., Galeev, Rosner & Vaiana 1979; Haardt, Maraschi & Ghisellini 1994; Svensson 1996; Nayakshin 1998a,b,c). In the framework of that model, the X-ray flux from the active region is very much larger than the radiation flux generated within the disk. Nayakshin & Melia (1997a), Nayakshin (1998b) and Nayakshin & Dove (1999) found that the radiation pressure from the X-rays of magnetic flares may be larger than the unperturbed gas pressure of the accretion disk atmosphere. Thus, we ought to incorporate the effects of the incident radiation pressure in our pressure balance calculations for generality.

The radiation force per hydrogen atom inside the reflecting layer,  $\mathcal{F}$ , is equal to

$$\mathcal{F}(\tau_t) = n_H \int_{-1}^{+1} \mu d\mu \int_0^\infty d(E/c) I(\mu, E, \tau_t) \sigma(E, \tau_t) \\ = (F_x/c) n_H \Delta\sigma(\tau_t), \quad (18)$$

where we introduced  $\Delta\sigma(\tau_t) \equiv F_x^{-1} \int \mu d\mu \int dE I \sigma$ , which has dimensions of a cross section ( $\sigma$  here is the total cross section per hydrogen atom). Note that this quantity can be positive as well as negative; a positive  $\Delta\sigma(\tau_t)$  corresponds to radiation force pointing upward, which would happen when the cross section for the interaction of matter with the reprocessed emission is larger than that with the X-rays. The equation for the pressure balance now reads

$$\frac{\partial P_{\text{gas}}}{\partial z} = -\frac{GM\rho}{R^2} \frac{z}{R} + \frac{F_x \Delta\sigma(\tau_t) n_H(z)}{c} + \frac{F_d \sigma_T n_H}{c}, \quad (19)$$

It is convenient to re-write this equation in terms of dimensionless quantities that will figure prominently in the

ionization and radiation transfer calculations. These are: the gas pressure normalized by the incident X-ray radiation pressure,  $\mathcal{P} \equiv cP_{\text{gas}}/F_x$ ; the differential Thomson depth,  $d\tau_t \equiv -n_e(z)\sigma_t dz$ ; and the compactness parameter  $l_x$  defined as

$$l_x \equiv \frac{\sigma_t F_x H}{m_e c^3}. \quad (20)$$

We will further introduce a dimensionless “gravity parameter”,  $A$ , for brevity of notations:

$$A \equiv \frac{R_g \mu_m}{2R m_e} \left(\frac{H}{R}\right)^2 l_x^{-1}, \quad (21)$$

where  $\mu_m$  is defined by  $\mu_m = \rho/n_H$  and  $H$  is the scale height of the SS73 accretion disk. The parameter  $A$  characterizes the strength of the gravity term relative to that of the X-radiation pressure in Equation (19). The hydrostatic balance equation is given by

$$\frac{\partial \mathcal{P}}{\partial \tau_H} = \left[ A \frac{z}{H} - \frac{\Delta\sigma}{\sigma_t} - \frac{F_d}{F_x} \right], \quad (22)$$

where  $d\tau_H \equiv -n_H \sigma_T dz = (n_H/n_e) d\tau_t$ .

### 3.4. Pressure boundary conditions

The solution of the hydrostatic balance equation (22) is subject to boundary conditions. The boundary condition on the top of the illuminated layer is  $P_{\text{gas}}(z = z_t) = 0$ , obviously (although note that if a hot corona is placed on the top of the illuminated layer, then  $P_{\text{gas}}(z = z_t) \neq 0$  – see Róžańska et al. 1999). Practically, we set  $P_{\text{gas}}(z_t)$  to a small fraction of the incident X-radiation ram pressure, i.e.,  $\mathcal{P} = 10^{-2} - 10^{-3}$ . The boundary condition on the bottom of the illuminated layer requires that the gas pressure be continuous across the interface between the illuminated layer and the accretion disk. Once the pressure profile in the disk is known, it is a relatively simple matter to iterate on the *a priori* unknown location of the top of the illuminated layer  $z_t$  in order to adjust the gas pressure on the bottom to match the disk pressure. However, one inherent problem here is that the vertical structure of the accretion disks is not necessarily well known (see, e.g., De Kool & Wickramasinghe 1999). For the gas-dominated accretion disks, we will simply assume that the density profile follows exponential law<sup>4</sup>:

$$\rho(z) = \rho(0) \exp[-(z/z_d)^2], \quad (23)$$

where  $z_d$  is the “average” scale height, which we approximate as  $z_d^2 = (2R^3 k_B / GM \mu_m) [T_d T_{\text{eff}}]^{1/2}$ , where  $k_B$  is the Boltzmann constant and  $T_d$  is the disk mid-plane temperature. In principle, one could resolve the vertical structure of the disk to a “better” precision by integrating the hydrostatic balance equation from the disk mid-plane up. However, the distribution of the disk viscous dissipation with height is not known (SS73 simply assumed it is proportional to the gas density), precluding the accurate determination of the temperature profile  $T(z)$  of the disk. Fortunately, as we will see later, this does not bring any serious complications except for a slight uncertainty in the exact value of  $z_b$ .

<sup>4</sup>Of course, this density profile is applicable only deep within the disk, where the X-ray heating is negligible, i.e., below  $\tau_t = 4$  by our choice.

We are less lucky in the radiation-dominated (RD) case, since there the boundary conditions are of a greater importance. To see this, consider the case in which the illuminated layer is completely ionized, so that the only source of opacity is the Thomson one. In this case,  $\Delta\sigma = 0$ , and the second term on the right in equations (19) and (22) is zero. Further, note that without the second term, equation (19) is exactly the equation for hydrostatic balance inside the disk. In the RD case, the gas pressure is negligible everywhere except for very near the edge of the disk. In other words, inside the disk, the gravity term is canceled by the intrinsic radiation pressure term (the last term in eq. 19 on the right). As we found, the illuminated layer does not extend very high in the RD case, e.g.,  $(z_t - z_b)/H \ll 1$ , so that the first term on the right in eq. (19) is again almost completely canceled by the last term. In other words, the net force is the difference of two very large terms, and hence it is rather sensitive to the location of the illuminated layer lower boundary  $z_b$ .

Another serious problem is that the gas density profile in an RD disk is uncertain to a much greater degree than in the case of a gas-dominated (GD) disk. As shown in SS73, if one completely neglects the gas pressure, then the density is constant with height all the way to  $z = H$  in RD disks. In order to significantly improve the SS73 approximation to the vertical disk structure, one needs to solve the energy balance equation for the accretion disk *simultaneously* with the pressure balance. This is a more difficult problem (and more model dependent) than the one we are attempting to solve in this paper (e.g., De Kool & Wickramasinghe 1999), and for this reason it is clearly outside of the scope of our present work. Therefore, at present, we make the *total* pressure continuous across the lower boundary and use the approximation of SS73 for the vertical pressure structure. Since we require the gas temperature to be equal to the disk effective temperature and since the radiation field incident on the lower boundary from the illuminated layer is quite close to the Planckian function, the radiation pressure is actually continuous through the boundary by our choice (see discussion below eqs. 13 and 14). Thus, if we match the total pressure on both sides of the boundary to within a very small difference, the gas pressure and density will also be continuous.

### 3.5. The Complete Iteration Procedure

In order to achieve static solutions for all the quantities in all vertical zones, we make the following steps:

- 1) First, we guess the location of the upper boundary of the illuminated gas  $z_t$ , and we also assume an initial intensity  $J(E, z)$  in all the spatial bins, usually simply equal to the sum of the incident X-ray intensity and the black body spectrum, and use it as an input to XSTAR in order to obtain the opacities. The initial value of the Eddington variable factors is assumed to be the isotropic value, i.e.,  $1/\sqrt{3}$ . Then, starting from the top of the illuminated layer, we solve for the gas pressure in the next zone using eq. (22). Given that value of  $P_{\text{gas}}$ , we call XSTAR with the initial illuminating spectrum. XSTAR provides on output the gas temperature, density, opacities, line and continuum emissivities for this zone. We repeat this step for the next zone (i.e., again solve for its pressure and then call XSTAR), until we reach the bottom of the transition

layer.

- 2) Having found the gas opacities and emissivities, we proceed to compute the radiation transfer as described in §3.1. At this step, we fix the opacities and emissivities at the value given by the previous iteration of XSTAR, and make 20-25 iterations of the radiation transfer calculations (made by an implicit differencing scheme) until the reflected spectrum converges. The variable Eddington factors are also continuously updated during this step.

- 3) At the same time, we check the consistency of the lower pressure boundary condition. In particular, we compare the pressure at the base of the illuminated layer (i.e., at  $z = z_b$ ) with the SS73 pressure at the same height. If the latter is larger than the former, we increase the value of  $z_t$  from the previous iteration; if not, we decrease it.

- 4) Now that we have the refined value of  $z_t$ , and the new ionizing spectrum in each bin, we repeat step (1) using the new values for  $z_t$ , the ionizing spectrum and the variable Eddington factors.

We continue to repeat these steps until a convergence is reached. We found that the best indicator of convergence is the matching of the boundary pressure at the base of the layer,  $P_b$  to the SS73 pressure at that height  $P_{ss}$ . We typically require that  $|P_b - P_{ss}| \lesssim 0.01 - 0.001$ . We also check that the temperature structure of the illuminated layer stops evolving to the same level of precision. Typically, we need to repeat the whole cycle 20 or more times, which translates into  $\sim$  a day of CPU of a 500 MHz PC for about 250 spatial zones and 400 photon energy points.

### 3.6. On the uniqueness of a hydrostatic balance solution

Figure (1) shows that due to the thermal instability, there are two, and sometimes even three stable solutions of the thermal and ionization balance equations for a given gas pressure and local ionizing spectrum when the gas pressure is in the range  $\mathcal{P} \simeq 0.1 - 0.5$  (equivalently,  $\Xi \simeq 2 - 10$ ). Thus, one *has to choose* a solution out of the several possible based on additional considerations.

The approach that would leave no ambiguities would be to supplement our ionization and radiation transfer methods with dynamical equations for the gas motions in the illuminated layer (e.g., Alme & Wilson 1974). Such an approach would delineate the different solutions automatically, since then one would follow the evolution of the gas density explicitly. For a given density (unlike given pressure), there is always a thermally stable, unique solution of the ionization and thermal balance equations (this can be seen from an always positive slope of the  $T$  versus  $\xi$  curve; see, e.g., Nayakshin 1998c, Fig. 5.2). In addition, inclusion of thermal conduction (e.g., Róžańska1999) can also forbid some of the otherwise stable solutions (see below).

Unfortunately, the numerical complexity of such an approach is prohibitive. The problem with adding the heat conduction to our code is that in our iterative process, we move from a known temperature in zone  $j$  to solve for temperature in zone  $j + 1$ , whereas thermal conduction requires knowledge of temperature in zone  $j + 2$  at this step. Writing a time-dependent code that would self-consistently treat the line cooling is also challenging and beyond the scope of the present work.

Given this, we should be able to find a way to single out a solution with some desirable property (e.g., within

a given temperature range) out of several possible solutions via our numerical methods. We discovered that the easiest way to accomplish this is to give XSTAR an initial temperature guess,  $T_{in}$  that is somewhat close to the temperature of the solution that we want to pick. This is due to the fact that XSTAR defines the temperature range where it will seek a solution in some interval around the initial temperature  $T_{in}$ . If there indeed exists a solution that is close to  $T_{in}$ , then XSTAR converges to that solution; if that solution does not exist, then XSTAR expands the interval until it finds a solution.

To avoid complications due to line cooling, we first demonstrate this method of separating the solutions with the example of a calculation in which all the resonant lines were assumed to be optically thin, i.e.,  $\tau_l \equiv 0$  for all lines in all spatial zones. Figure (2) shows the gas temperature as a function of the Thomson optical depth for two tests. In both tests, the X-ray flux with  $F_x = 10^{16}$  erg  $s^{-1}$   $cm^{-2}$  is incident in the direction normal to the reflecting layer. Other parameters have the following values:  $\Gamma = 1.9$ ,  $A = 1.2$ , and  $l_x = 0.01$  (given that, one can compute the disk vertical height scale  $H$ ; for simplicity, we assume that the bottom of the reflecting layer is located at  $z_b = H$  for the tests in this section; this does not affect any of our conclusions here). The solid curve was computed for the case when an initial temperature guess for each zone is equal to  $kT = 3$  keV. This method ensures that whenever there are multiple solutions, the hottest one is chosen. In terms of the optically thin S-curve shown in Figure (1), this simulation yields the transitions from the hot Compton-heated branch to the medium stable branch via line (c-d), and then via line (e-f). The dotted curve shows results of a test when an initial gas temperature is close to  $T_{eff}$ . As we found, this method always leads to a solution with the smallest possible temperature, which corresponds to the discontinuity occurring via line (a-b) in Figure (1).

In Figure (3) we show three tests for the same parameter values, but with the resonance line optical depths self-consistently calculated as described in §3.2. The long-dashed curve shows the results of a calculation with the initial temperature for each bin  $T \simeq T_{eff}$ . As with the dotted curve of Fig. (2), the cold solution is recovered rather quickly at  $\tau_t \simeq 0.07$ , as soon as it becomes available. Contrary to the optically thin case shown in Fig. (2), however, the next zone jumps back to the hot solution. The reason for this is line cooling. For a given bin, the line optical depths are calculated by summing over the line depths of all the previous bins. Since the material is highly ionized for all zones preceding the one with  $T \simeq T_{eff}$ , there is little line optical depth for this zone, and thus we can use the S-curve generated for optically thin lines (solid curve in Fig. 1). However, for certain lines the optical depth of the first cold zone turns out to be significant, and therefore cooling for all the material with  $\tau_t \gtrsim 0.07$  cannot be assumed to be (line-) optically thin anymore. We then need to refer to the other two curves in Fig. (1) that were calculated for a non-zero line optical depth  $\tau_l$  (where it was assumed for simplicity that all the lines have a given value of  $\tau_l$ ). In particular, the longed-dashed curve in Figure (1), shows that there is no cold solution with  $\Xi \simeq \Xi_b$ , where  $\Xi_b$  is the pressure ionization parameter at point (b). The only ac-

ceptable solution is the hot solution, which then explains why the temperature in the next zone jumps back to the Compton equilibrium. Note that a finer (than the one we used) zoning around this point will not remove this behavior, since this behavior is physical rather than numerical. The two other dips in temperature around  $\tau_T \simeq 0.135$  and  $\tau_T \simeq 0.155$  in the dashed curve in Fig. (3) are caused by similar effects due to different lines.

Since the sharp dips in the temperature will cause a strong conductive heating, the cold temperature guess method seems to be inappropriate. Further, as discussed by London et al. (1981), the effects of the line cooling may lead to a non-steady behavior in the illuminated layer. Indeed, the layer at  $\tau_t \simeq 0.07$  is very much denser than the layer immediately below it, and thus it is convectively unstable.

The dotted curve in Figure (3) was computed assuming always high initial temperature ( $kT_{in} = 2$  keV). This curve produces one sharp dip in temperature at  $\tau_t \simeq 0.17$ . At this point, only the cold solution exists. In the next spatial zone, due to the larger line depth, there appears a solution with the intermediate temperature,  $kT \sim 100$  eV, which is found by XSTAR since the initial guess for  $T$  is high. However, there also exists a colder solution, which is seen in the solid curve presented in the same Figure. The latter curve was computed by providing XSTAR with the initial temperature equal to that of the previous zone multiplied by 1.5. If the conductive heating was taken into account, it would force the gas in the zone with the large jump in temperature to cool and so it would lead to a solution close to the solid line. We show in the Appendix that the conductive heating is always small except for regions that are close to the temperature discontinuities. The latter regions are always optically thin ( $\Delta\tau_t \lesssim 10^{-3}$  at most, see Appendix), and hence they are unimportant from the point of view of the radiation transfer and spectral reprocessing.

Out of these three methods of picking a solution, the one based on the temperature of the previous zone is the most physical in the sense that it has no sharp dips or spikes in temperature except for the bump with the magnitude of about 2 in the region around  $\tau_t \sim 0.17 - 0.2$  (Similar features were earlier seen in the work of Ko & Kallman 1994). Therefore, we adopt this method in the rest of the paper.

## 4. TESTS

### 4.1. Setup

A systematic investigation of the reflected spectra as a function of the accretion rate,  $\dot{m}$ , and the magnitude of the X-ray flux,  $F_x$ , is our eventual goal. Solving this problem consists of two steps: (1) resolving the density and temperature profile of the illuminated layer; (2) determination of how this profile influences the radiation transfer in the illuminated layer, i.e., the reflected spectra. Step (1) is not necessarily difficult, but it depends quite sensitively on the assumptions about the geometry of the X-ray emitting source (or sources). For example, if X-rays are produced in magnetic flares, then, because the geometry of the problem is no longer plane-parallel, there is a possibility that a local wind is induced (see §6 on this). We clearly cannot treat this situation within our current static approach. Another possibility is that the accretion disk is

not described by the standard model, such that  $H/R$  is different from the SS73 value, which then changes the gravity parameter  $A$ . In other words, we have a large parameter space to investigate, and such an investigation clearly goes beyond the scope of this paper.

At the same time, for a fixed  $\Gamma$ , step (2) depends, to a large degree, on two parameters only. One of these is the Thomson depth of the Compton-heated layer,  $\tau_h$ , and the other is the ratio of the illuminating flux to the disk intrinsic flux,  $F_x/F_d$ , since this ratio determines the actual value of the Compton temperature  $T_c$ . Therefore, as a first attempt towards understanding of the effects of the thermal instability on the reflected spectrum, we set up simple tests that allow us to cover a range of values of  $\tau_h$  and  $T_c$  by varying one parameter at a time, thus isolating dependence of the reprocessed spectra on that particular parameter.

We assume the following initial setup. We fix the accretion rate at a value of  $\dot{m} = 10^{-3}$  (the disk is gas-dominated for such a small accretion rate), the incident X-rays to be isotropic for simplicity, the coronal dissipation parameter  $f = 0$  (no dissipation in the corona; see Svensson & Zdziarski 1984 for a definition), the black hole mass to  $M = 10^8 M_\odot$ , and the incident X-ray flux (projected on the disk surface) to  $F_x = 10^{16}$  ergs s $^{-1}$  cm $^{-2}$ . For these values of parameters,  $F_x/F_d \sim 1.6 \times 10^3$ , and the gravity parameter  $A$  equal to  $A_0 = 1.66 \times 10^{-3}$ . To study the effects of the thermal instability, we artificially vary the parameter  $A$  from this “true” value (other parameters of the problem will later be varied as well). The rest of our methods, i.e., the radiation transfer, the boundary conditions between the disk and the illuminated layer are unchanged, that is the same as we will later use in fully self-consistent calculations (§5).

#### 4.2. *Hydrostatically stratified vs. fixed density atmospheres*

It is beneficial to start by comparing the results of our self-consistent calculations with those obtained with the fixed density approach, since the latter dominated the literature on the topic during the past decade (e.g., Ross and Fabian 1993; Życkiet al. 1994; Ross et al. 1997, 1999). The most important parameter in photo-ionization calculations when the gas density is constant is the density ionization parameter  $\xi$  (eq. (2)). In the case of our calculations that include the hydrostatic balance, the ionization structure of the illuminated layer depends most sensitively on the “gravity parameter”  $A$ . The upper panel of Figure (4) shows temperature of the illuminated layer as a function of the Thomson depth into the layer for several values of the gravity parameter  $A$ , whereas the lower panel of the same figure shows the gas temperature for different values of the density ionization parameter  $\xi$  (both the fixed density cases and the self-consistent cases are computed with our code under equal conditions and parameter values except for the gas density structure).

In short, the two sets of temperature curves have almost nothing in common. The self-consistent solution avoids the regions in temperature that correspond to a negative slope in the “S-curve” (cf. Fig. 1), i.e., the unstable regions, whereas they are unphysically present in the fixed density cases (Fig. 4). To see that the fixed density solutions are indeed unphysical, notice that since the gas den-

sity is constant, the gas pressure is directly proportional to its temperature. Hence, on the top of the illuminated atmosphere, instead of decreasing to zero, the gas pressure exceeds that on the bottom of the layer by a factor as large as a few hundred. The constant density calculations are out of the pressure balance, and therefore will not exist in reality.

The temperatures that are allowed in the self-consistent solutions are those with the positive slope in the “S-curve”; the amount of Thomson depth they occupy depends on the pressure balance. Going from the low illumination (high  $A$ ) cases to the high illumination limit ( $A \ll 1$ ), the amount of the hot material increases, as it should, but the temperature of the Compton-heated layer does not change considerably, except for the case when the hot layer becomes Thomson thick. If one assumes that the hot material is ionized enough to neglect line and recombination cooling, then it is possible to analytically find the temperature,  $T_t$ , below which the Compton heated solution ceases to exist (see §IVb in KMT). The value of  $T_t$  is  $T_t = 1/3T_c$ , i.e., a third of the Compton temperature at the very top of the illuminated layer. The upper panel of Figure (4) shows that this transition temperature is indeed close to a third of the maximum temperature if  $A \gtrsim 1$ . In the opposite limit, the Compton-heated layer is optically thick and thus the ionizing spectrum is actually different at the surface and at the transition; the simple analytical theory would need to take this fact into account in order to be more accurate.

In contrast, the fixed density calculations incorrectly predict that not only the Thomson depth of the hot layer, but its temperature, too, changes. This fact has obvious consequences for the reflection component and the iron lines, as we will see below.

Figure (5) shows the gas temperature, the “radiation pressure force multiplier”  $\Delta\sigma$ , the gas pressure and the height above the bottom of the illuminated layer for the self-consistent test with  $A = 0.01$ . Fig. (5d), in particular, demonstrates that the density profile cannot be assumed to be a Gaussian, because, in a rough manner of speaking, there are two height scales – one for the cold part of the illuminated layer, and another for the Compton-heated part.

Comparing the temperature profiles shown in the upper panel of Fig. (4) with results of Ko & Kallman (1994), Rózańska and Czerny (1996), Rózańska (1999), one finds that the intermediate stable solution occupies a smaller Thomson depth relative to the Compton-heated solution than found by these authors. This small Thomson depth is also somewhat unexpected because the part of the S-curve between points (e) and (d) in Fig. (1) is not “small”, i.e., it corresponds to a change in the gas pressure by a factor of  $\sim$  few. Panel (b) of Figure (5) shows that  $|\Delta\sigma| \ll 1$  everywhere except for the region right below the interface between the hot and the cold solutions, where the X-ray radiation pressure force has a sharp peak. The direction of the force is always down, i.e., in the same direction as the disk gravity, because the soft X-ray opacity dominates over the opacity to the quasi-thermal disk spectrum. Panel (c) of Figure (5) shows that due to this X-ray pressure, the gas pressure increases almost discontinuously once the temperature falls to the cold (or the intermediate) stable

branch values. Thus, the intermediate stable branch of the S-curve can be passed very quickly and even “skipped” because of the additional radiation pressure.

Also note that the radiation pressure force due to the incident X-rays minus that due to the reprocessed flux is small in the integrated sense. This allows us to approximately neglect this term in the hydrostatic balance equation (22). If the transition from the hot to the cold solution occurs at  $\Xi_t \sim \text{few}$ , then equation (22) tells us that the Thomson depth of the hot layer is roughly

$$\tau_h \sim (\Xi_t A)^{-1} \quad (24)$$

In accordance with this simple estimate, Fig. (4) shows that larger values of  $A$  result in lower values of  $\tau_h$ , although the dependence of gravity law on the height  $z$  makes this behavior more complex than equation (24) predicts. A much better analytical theory describing the temperature structure arising from the self-consistent calculations can be obtained by using the analytical theory of KMT and the equation for the hydrostatic balance; we will present this theory in a future paper.

#### 4.3. Angle-Averaged Reflection Spectra

We will now discuss the reprocessed spectra that correspond to the temperature profiles shown in Fig. (4). Figure (6) shows the reflected spectra for both the constant density cases and our self-consistent calculations in the important medium and hard X-ray energy range. These spectra are shifted with respect to each other to allow easy visibility of the line. Also, in order to expose the true strength of the line and the reflected continuum, we re-plotted several of these curves with their correct normalization in Fig. (7). Finally, for completeness, Fig. (8) shows the same spectra as in Fig. (7) in the broader photon energy range. It is clear from Fig. (8) that the reflected spectra in the “thermal” energy range (e.g.,  $\sim 10 - 100$  eV for the chosen X-ray flux), are not accurately computed (as they never were in previous works on the X-ray reflection). In order to improve the treatment of the radiation field at these energies, one would need to take into account stimulated emission and other many-body processes in the cold layers of the illuminated gas, which we plan to do in our future work. Fortunately, spectra above  $E \gtrsim 1$  keV should not be affected by this.

The critical information needed to understand the results presented herein is that for the relatively hard X-ray spectrum such as the one with  $\Gamma = 1.9$ , most of the iron atoms in the Compton heated layer turn out to be nearly completely ionized, and thus both line emission and photo-absorption in this material are very weak. We can define the following limiting cases to describe the behavior of the reprocessing features.

**HIGH ILLUMINATION LIMIT.** When the gravity parameter  $A$  is small, i.e.,  $A \lesssim 0.1$  no easily visible reprocessing features result from the illuminated slabs. The physics of this effect is rather transparent. When the Compton-heated layer is Thomson thick, the X-rays incident on the disk atmosphere are reflected back before they can reach the cooler layers where the material is less ionized and where they could be absorbed and reprocessed into line or thermal radiation. Further, most of

the photons will be reflected back by the Thomson depth  $\tau_t \sim 1 - 2$ , which then means that the Compton scattering changes the photon energy only slightly unless the photon is mildly relativistic ( $E \gtrsim 50$  keV). Therefore, it is to be expected that for photons of energy smaller than the energy corresponding to the peak in the neutral reflection component, i.e.,  $E \sim 30$  keV, the completely ionized material represents a perfect mirror (only the photons’ angle changes after the scattering). Above  $E \sim 30$  keV the photons are downscattered in a way very similar to that in the neutral reflection, so that the reflected spectrum above these energies is essentially unchanged (see Fig. 7).

**LOW ILLUMINATION LIMIT.** The low illumination case can also be called the “strong gravity limit”, when  $A \gg 1$ . As Figure (4) shows, the Thomson depth of the Compton layer is much smaller than unity under these conditions, and hence its existence is of no noticeable consequence for the reflected spectra. The latter are basically the same as the reflection spectra obtained in the classical studies of the neutral X-ray reflection as far as the medium to hard X-ray photons are concerned, (e.g., Basko et al. 1974; Lightman & White 1988, Magdziarz & Zdziarski 1995). The iron line is rather narrow with centroid energy  $\simeq 6.4$  keV, and there is rather strong absorption edge above  $\sim 7 - 8$  keV.

**MODERATE ILLUMINATION.** To a zeroth order approximation, the intermediate cases, when illumination is neither very strong or very weak, i.e.,  $0.1 \lesssim A \lesssim 10$ , represent a combination of the low and the high illumination cases. The Thomson depth of the Compton-heated layer is moderate ( $\tau_h \lesssim 1$ ), so the X-rays propagating in the downward direction have a fair chance to reach the cold layers. The X-rays incident on the latter have spectrum similar to the incident one (except for the high energy end of the spectrum), and therefore the spectrum that will be reflected off the cold layers (i.e., the one propagating in the upward direction at the interface between the Compton and the cold layers) will resemble the cold non-ionized reflection.

The Compton scattering of the “reflection hump” in the hot layers will not broaden it substantially. However, the effects of Compton scattering in the hot layers are quite pronounced for the energy range from about  $10 \times kT_{\text{eff}}$  to  $\sim 10$  keV, because most photons in this energy band would be absorbed in the standard cold reprocessing (see, e.g., Fig. 5 in Magdziarz & Zdziarski 1995, or the lower solid curve in Fig. 8). The larger the Thomson depth of the hot layer, the larger is the number of photons of this low energy ( $< 10$  keV) band that are Compton-reflected back within the *hot upper layer*, reducing the apparent strength of the “reflection hump”. One should note that the influence of the Compton-heated layer on the X-ray reprocessed spectra was already discussed by Basko, Sunyaev & Titarchuk (1974), but this issue was not addressed at all in later works on X-ray reflection (and, in fact, neither was the work of Basko et al. (1974)).

It is worthwhile to point out that the iron line centroid energy remains at  $E = 6.4$  keV for all of our self-consistent calculations. Similarly, the position of iron edge remains the same. These reprocessing features only get weaker, and thus less visible as the illumination increases ( $A$  de-

creases). One can also note that there is a certain amount of broadening of the line by Comptonization. It is possible that this broadening can actually be detected if it is present in the data (Done 1999, private communications). In order to accurately model line Comptonization, it is desirable to perform higher resolution calculations using an exact Klein-Nishina scattering kernel, which we plan to do in the future.

#### 4.4. Comparison to the constant density reflection spectra

If the illuminating flux is low, then the material is non-ionized in both self-consistent and constant density calculations, and its temperature is close to the effective one. Thus, the spectra in the low illumination limit discussed in §4.3 should be similar to those computed assuming constant gas density for  $\xi \lesssim 100$  or so (e.g., Lightman & White 1988; Życkiet al. 1994; Magdziarz & Zdziarski 1995). Likewise, if the illuminating flux is very high, the gas temperature is close to the Compton one, and hence irrespectively of whether the gas density is fixed or found from hydrostatic equilibrium, the reflected spectra have very little iron line or edge. This is the limit of the Compton reflection, i.e., the one without photo-absorption (cf. Basko et al. 1974, White et al. 1988). The reflected spectrum has virtually the same power-law index as the incident X-ray continuum, and only differs above  $E \gtrsim$  few tens of keV. Figures (6) and (7) confirm these considerations.

However, the differences in the reprocessing features between the self-consistent calculations with moderate values of the gravity parameter, i.e.,  $0.1 \lesssim A \lesssim 10$  and the constant density calculations are truly remarkable (see Figs. 6 and 7). The former shows that the He-like iron line at  $\simeq 6.7$  and H-like line at  $\simeq 6.9$  keV never dominate over the “cold” iron line at 6.4 keV, whereas the fixed density calculations predict that at  $\xi \gtrsim 800$  the iron line at 6.7 keV will dominate. In addition, under the constant density assumption, the Equivalent Width (EW) of the iron lines in the mildly ionized case can be larger by a factor  $\sim 2.5$  compared with the line’s EW in a neutral material (see Matt et al. 1993). On the contrary, our calculations presented here show that solving for the pressure balance leads to the opposite behavior of the EW. Going from low illumination cases (large  $A$ ) to higher illumination (lower  $A$ ), one finds that the strength of the iron lines rapidly decreases, and the absorption edge gets less noticeable (cf. Fig. 6).

#### 4.5. Reflection at Different Viewing Angles

Figure (9) shows the reflected spectra at three different viewing angles for the test with  $A = 1$ . It is seen that the reprocessing features are strongest for the angle closest to the normal, and that they almost disappear at large angles. The explanation for this effect is rather straight forward: the Thomson depth of the Compton heated layer, when viewed at an angle  $i$  with respect to the normal is  $\tau_h(\mu) = \tau_h/\mu(i)$ , where  $\mu(i) \equiv \cos i$ , and  $\tau_h$  is the Thomson depth of the Compton layer as seen at angle  $i = 0$ . Further, since one only receives emission from material within one optical depth (roughly speaking), at large inclination angles only the Compton heated layer contributes to the reflected spectrum, and therefore no visible iron lines ap-

pear. This effect should be important in modeling the iron lines from accretion disks that are seen almost edge-on. Unless the optical depth of the completely ionized layer is very close to zero, no iron line should be observed in such systems (barring a more distant putative molecular torus).

#### 4.6. Effects of Different X-ray Incidence Angles

Figure (10) shows the temperature profile and the angle averaged spectra computed for  $A = 0.1$ ,  $F_x = 10^{16}$  erg s $^{-1}$  cm $^{-2}$ , and  $\dot{m} = 10^{-3}$  for two different values of the X-ray incident angle  $\theta^5$ . The solid curve corresponds to  $\cos\theta = 15/16$  (i.e., almost normal incidence), whereas the dotted curve corresponds to  $\cos\theta = 1/16$  (i.e., almost parallel to the disk surface). It is interesting to note that the temperature profiles are rather similar for moderate Thomson depths. We interpret this effect as due to the fact that the X-rays are isotropized by the time they penetrate to  $\tau_t \sim 1$ , so that the incident angular distribution does not matter.

In the layer near the surface, however, the difference is quite noticeable. In the case of the normal incidence, the gas temperature is only  $kT = 3$  keV on the very top of the layer, while it is  $kT = 5.2$  keV for the grazing angle of incidence. The difference is easily explained by the fact that the Compton temperature is approximately equal to

$$T_c \simeq \frac{T_x J_x + T_{\text{eff}} J_{\text{ref}}}{J_x + J_{\text{ref}}}, \quad (25)$$

where  $J_x$  and  $J_{\text{ref}}$  are the *angle integrated* intensities of the X-ray and the reflected radiation (e.g., see Begelman, McKee & Shields 1983). We should now recall that the X-ray flux  $F_x$  is the flux projected on the direction normal to the disk. Therefore,  $F_x \propto \mu_i J_x$ , whereas  $F_{\text{ref}} \propto J_{\text{ref}} \mu_{\text{ref}}$ . Note that  $1/\sqrt{3} < \mu_{\text{ref}} < 1$ , since the reflected radiation is clearly less isotropic than a truly isotropic field that would have  $\mu = 1/\sqrt{3}$  and yet less beamed than a pencil beam escaping in the direction close to normal. Taking into account that  $F_{\text{ref}} \equiv F_x + F_d \simeq F_x$ , for X-rays that are normally incident on the disk,  $T_c \simeq T_x/(1 + \mu_{\text{ref}})$ ; for grazing angles of incidence with  $\mu_i \ll 1$ ,  $T_c \simeq T_x/(1 + \mu_i/\mu_{\text{ref}}) \simeq T_x$ . This is the reason why the gas temperature is hotter for larger incidence angles. One can also note that this region with  $T \simeq T_x$  will not extend to very large  $\tau_t$ , since at  $\tau_t \sim \mu_i^{-1}$  most of the incident X-rays will have been scattered at least once, which makes the X-radiation field more nearly isotropic. This latter fact is clearly seen in Figure (10a).

Turning to the difference in the reflected spectrum, Figure (10b) demonstrates that the larger angles of incidence produce more hard X-ray continuum and the reprocessing features are weaker than in the case of nearly normal incidence. This effect is due to a larger number of scatterings that the incident photons suffer before they reach the cool line-producing layers in the former versus the latter case; i.e. when the X-rays come in at a large angle they are more likely to be reflected back before they can be photo-absorbed in the cold material.

Finally, we should mention that for this particular calculation, we turned off the X-ray pressure altogether, i.e., assumed  $\Delta\sigma \equiv 0$  in equations (19) and (22). As a result,

<sup>5</sup>These spectra were computed with 400 photon energy bins; i.e., with a lower resolution than most of the other calculations presented in our paper.

the intermediate stable state, i.e., the one with  $kT \sim 150$  eV, occupies a considerably larger range of the Thomson depth in Fig. (10) than it did earlier for the tests shown in Fig. (4), when we self-consistently computed  $\Delta\sigma$ . This therefore confirms that it is indeed the X-ray pressure that “compresses” the intermediate stable region (see §4.2) compared to calculations of Ko & Kallman (1994) and Róžańska(1999).

#### 4.7. Different indices of the ionizing radiation

Figure (11) shows how the temperature of the illuminated layer varies with the hardness of the incident X-rays while all the other parameters are held fixed. The fact that the maximum gas temperature increases with decreasing  $\Gamma$  is easily understood because the Compton temperature of a harder spectrum is higher. In addition, the harder the spectrum, the larger is the optical depth of the Compton heated layer, because it takes more scatterings to bring the average photon energy down such that the low temperature equilibrium states will become possible. Also note that for a steep spectrum, i.e., for  $\Gamma \gtrsim 2.2$ , the gas temperatures in the range  $\sim 200 - 1000$  eV become allowed (because for such a spectrum the S-curve actually has a positive slope at these temperatures), whereas they are forbidden for harder spectra.

Because of these differences in the temperature profile, it comes as no surprise that the reflected spectra are very different for hard and soft spectra. In Figure (12) we show the reprocessing spectra corresponding to the five tests shown in Fig. (11). The hardest spectrum, i.e.,  $\Gamma = 1.5$  shows very little iron line emission. It seems intuitively clear that when one adds this spectrum to the illuminating X-ray spectrum, the line and the reflection component will be barely discernible. For a soft X-ray spectrum, however, not only the 6.4 keV iron line is stronger, but there is a strong 6.7 keV line as well.

### 5. RADIATION-DOMINATED DISKS

We now show several tests for a radiation-dominated accretion disk where the parameter  $A$  was equal to its nominal value as defined by equation (21). Figure (13) shows the gas temperature profiles and the reprocessed spectra for two values of the incident X-ray flux ( $10^{16}$  erg cm $^{-2}$  s $^{-1}$  for the long-dashed curve, and  $10^{15}$  erg cm $^{-2}$  s $^{-1}$  for the rest of the curves)<sup>6</sup>.

Let us first concentrate on the long-dashed and the dotted curves. These differ only by the absolute magnitude of the illuminating flux. The self-consistent value of  $A$  for these tests is  $A = 6.34 \times 10^{-2}$  and 0.634 for the long-dashed and dotted curves, respectively. If we now compare these curves with the sequence of curves shown in the upper panel of Fig. (4), then we can observe that the radiation-dominated (RD) illuminated layers have much thicker Compton-heated regions than Fig. (4) would predict for similar values of  $A$ . The difference is due to the fact that the disk radiation force is strong even above  $z = H$  for a RD disk: the radiation force due to the disk intrinsic emission cancels most of the gravitational force in the vicinity of the disk surface (see equation 22 and §3.4). It is then convenient to introduce a “modified gravity param-

eter”  $A_m$  defined as

$$A_m \equiv A - \frac{F_d}{F_x}, \quad (26)$$

which then allows one to rewrite the equation for the hydrostatic balance for the illuminated layers above the RD disks as

$$\frac{\partial P}{\partial \tau_H} = \left[ A_m + A \frac{z - H}{H} - \frac{\Delta\sigma}{\sigma_t} \right]. \quad (27)$$

In the simulations presented in figure (13), the values of  $A_m$  were  $\simeq 2 \times 10^{-3}$  and  $2 \times 10^{-4}$ , for the dotted and long-dashed curves, respectively. In general, both terms ( $A_m$  and  $A$ ) are important in establishing pressure balance, so that the classification of the reflected spectra by only one parameter  $A$  is not as straight forward as it was for a gas-dominated disk (§4). Nevertheless, the behavior of the reflected spectra with  $A$  is qualitatively the same.

To investigate the importance of cooling due to the disk intrinsic flux, we set up two additional calculations. We kept  $A_m$  and  $A$  the same as for the dotted curve in Figure (13), but increased the intrinsic disk flux by factors 4 and 12 for the short-dashed and solid curves, respectively. This test demonstrates that the usually unstable temperature region between  $\sim 200$  eV and 1 keV can become thermally stable not only due to a soft X-ray incident spectrum (see §4.7), but also due to a large UV flux. As one can deduce from equation (25), the large intrinsic disk flux makes the maximum Compton temperature equal to  $T_c \simeq T_x F_x / F_d \ll T_x$ . This means that the ionized layer may have a relatively low temperature. When this temperature is below  $\sim 1$  keV, the reflected spectrum will contain features characteristic of “highly ionized” reprocessing (if the layer is somewhat optically thick), even though the ionizing spectrum is hard, in contrast to the results obtained for  $F_x / F_d \gg 1$  (cf. §4.7).

### 6. GAS EVAPORATION AND OTHER EFFECTS

So far we have been dealing with the problem of X-ray illumination in the context of a plane-parallel geometry where the X-rays come from infinity at a given incidence angle. Some of the possible geometries for the X-ray source and the accretion flow are not very far from this setup, while others may require solving a dynamical rather than a static problem. For example, if the X-ray source is located at some height above the black hole (“lamp post model”), as for example, in Reynolds and Begelman (1997), then the reprocessed spectra can be obtained by our methods if one also takes into account the variation in the ionizing flux  $F_x$  and the incident angle with radius. One would then calculate the reflected X-ray spectra for a grid of radii and then integrate over the disk surface.

However, a difficulty that cannot be resolved by our methods appears in the context of an accretion disk model where X-rays come from localized magnetic flares (e.g., Galeev et al. 1979; Field & Rogers 1993; Haardt et al. 1994, Nayakshin 1998c; Nayakshin & Dove 1999). This difficulty is that the problem becomes not static because evaporation of the material into a *wind* may become important.

Let us elaborate a little on this issue. As we mentioned, the thermal gas pressure of the Compton-heated

<sup>6</sup>These tests are conducted with 400 energy points as well.

layer cannot drive a wind out to great distances because the Compton temperature  $T_x \lesssim 10^8$  K is much below the virial temperature ( $T_{\text{vir}}$  of the gas in the inner disk  $T_{\text{vir}} = 2.7 \times 10^{12} r^{-1}$  K (see also Begelman, McKee & Shields 1983)). Similarly, the X-radiation for a sub-Eddington accretion rates (which we implicitly assumed here) cannot drive a global wind. Finally, line-driven winds (e.g., Proga 1999; Proga, Stone & Drew 1998) also cannot remove the Compton heated material since it is highly ionized and the line pressure force is basically zero. What the X-radiation pressure and the thermal pressure can do is to move the Compton-heated gas upwards or side-ways on distances of the order of few disk height scales  $H$  (one can check that moving the gas farther is counter-acted by the gravity and hence cannot be done). As far as we can see, this fact is of no consequence in the case of a single central X-ray source, whether it is located above the black hole or it is in the disk plane (e.g., Fig. 2 in Dove et al. 1997), since the typical dimensions of the X-ray illuminated region are  $\sim R \gg H$ .

In contrast, moving the hot gas away from a magnetic flare, the source of the illuminating X-rays, on the distance of order few  $H$  may be quite significant for the disks with flares, because most of the X-ray reprocessing will be done within this distance from the flare (see Fig. 1 in Nayakshin & Dove 1999 for an illustration). Once far enough from the flare, the gas will cool and settle down on the disk without much observational consequences. At the same time, the removal of the Compton-heated gas away from the flares reduces the value of the Thomson depth below the values calculated in this paper. Therefore, value of the gravity parameter  $A$  alone does not define the reflected spectra in the case of a magnetic flare, and future calculations, including gas dynamics are needed.

Fortunately, the reflected spectra depend most sensitively on the Thomson depth,  $\tau_h$ , of the Compton layer between the source of X-rays and the cold material, irrespective of whether a particular value of  $\tau_h$  is obtained in a static situation or in the "local wind". The wind velocity is comparable but somewhat larger than the thermal sound speed of the Compton-heated gas (see §III of McCray & Hattchet 1975 in the context of a stellar X-ray induced wind), which is only  $c_{\text{hot}} \simeq 3 \times 10^{-3}$  of the speed of light. Because the gas in the wind will probably be Compton-heated, so that line opacities and emission are not important there, we do not expect any significant effects due the gas bulk motions on the radiative transfer.

Accordingly, the X-ray reprocessing spectra should be very similar to the ones we obtained in this paper, covering the same low, moderate and high illumination limits, but the relation of these limits to the accretion disk and flare parameters (e.g.,  $\dot{m}$ ,  $F_x$ , size of the flare, etc.) is yet to be clarified.

## 7. SUMMARY

We now summarize the important points about X-ray reprocessing and iron line emission emerging from the calculations presented in this paper. We also discuss several observationally important issues where our methods should find useful applications.

1. The thermal ionization instability plays a crucial role in determining the density and temperature structure of

the illuminated gas. Its effects can be taken into account by a proper treatment of the hydrostatic balance or dynamics of winds if the latter are important. Because of a (nearly) discontinuous behavior of the gas density and temperature caused by the thermal instability, one may not assume the illuminated gas to have either a constant or a Gaussian density profile.

For **hard X-ray spectra** with  $\Gamma \gtrsim 2$ , and large X-ray flux (i.e.,  $F_x/F_d \gg 1$ ), the thermal instability "forbids" the illuminated layers from attaining temperatures in the range from  $\sim 200$  eV to  $\sim T_c/3$  typically  $\sim$  few keV. Temperatures in the intermediate range  $\sim 80 - 200$  eV are allowed, but due to the X-ray radiation pressure effects, the layers with these intermediate temperatures occupy a small Thomson depth and thus contribute little to the reflected spectra. The major contributor to the reprocessing features (lines, edges and the characteristic reflection bump itself) is the cool layer with temperature close to the effective temperature for the given X-ray and disk fluxes. The overall structure of the illuminated layer is then approximately two-phase one (neglecting the intermediate temperature layer): (i) the Compton-heated "skin" on the top of the disk, and (ii) cold, dense, and thus typically weakly ionized layers below the hot skin.

The iron is completely ionized in the Compton-heated material (for hard spectra), and thus the only important radiative processes there are Compton scattering and bremsstrahlung emission. As a result, the existence of the hot material always reduces the strength of the reprocessing features, because the incident X-rays may scatter back (and out of the disk atmosphere) before they reach the cold layers where atomic processes could imprint the characteristic reprocessing features. The Thomson depth,  $\tau_h$ , of the Compton-heated illuminated layer is controlled by the gravity parameter  $A$ , whose values distinguish the following characteristic cases:

- Low illumination, i.e., high values of  $A$  ( $A \gg 1$ ), which result in weakly ionized matter and lead to  $\tau_h \ll 1$  and hence to iron lines, edges and continuum reflection characteristic of neutral material.
- Moderate illumination, which corresponds to values of  $A$  in the range  $0.1 \lesssim A \lesssim 10$ , and produce moderately thick Thomson-heated layers. As far as the reflected continuum is concerned, the reprocessed spectrum represents a combination of that for the high and low illuminated cases discussed above. This may not be true for the iron lines, though, because Compton scattering of the line photons in the hot layer can be very effective in removing these from the line into the continuum (Done 1999, private communications). Further work is needed in order to understand how this moderate illumination limit will appear when observed by a particular instrument. We believe that because the Fe atomic features are created in the cold nearly "neutral" material, and yet their normalization is lower than that of standard neutral reflection, some narrow band X-ray telescopes may confuse the mildly illuminated reflector covering a full  $2\pi$  solid angle with a *non-ionized* reflector covering a fraction of  $2\pi$ .
- High illumination ( $A < 0.1$ ). X-radiation ionizes a substantial amount of material, so that the Compton-heated layer is Thomson-thick. Very little of either of the 6.4, 6.7

or 6.9 keV iron lines are created in this layer because few X-ray make it through to the cold disk material. Thus, the reprocessing features, except for the roll-over at few tens keV due to the Compton down-scattering are wiped out of the reflection spectrum. The latter is a power-law with a similar index as the incident one for  $E \lesssim 30$  keV, and can be undetectable in the lower energy data.

- The evolution of the reflection component and the iron lines from the weak illumination limit to the strong illumination limit is monotonic and in no point does the spectrum exhibit observational signatures of “highly ionized” matter (as do the spectra of the constant density studies), because the Compton layer is completely ionized and the line-creating material is very cold, effectively neutral. This is to be contrasted with the predictions of constant density models, where the EW of the line and its centroid energy increases with ionization parameter  $\xi$  (e.g., Ross & Fabian 1993; Matt et al. 1993; Życki et al. 1994; Ross et al. 1999).

**2.** Ionized iron lines and strong absorption edges can nevertheless be produced under the following conditions:

- If  $A \ll 1$ , and the incident X-ray spectrum is steep, as in soft states of GBHCs, i.e.,  $\Gamma \gtrsim 2$ , then the Compton temperature even on the top of the reflecting layer can be lower than  $\sim 1$  keV, which can then lead to the appearance of 6.7 and 6.9 keV iron lines.

- If  $A \ll 1$ , and the incident X-ray spectrum is hard,  $\Gamma \lesssim 2$ , but the disk intrinsic flux exceeds the X-ray illuminating flux, i.e.,  $F_d \gg F_x$ . This again lowers the Compton temperature of the hot layer and hence could yield ionized lines and strong absorption edges.

**3.** Reflected spectra viewed at larger angles relative to the disk normal always contain less reprocessing features (e.g., lines and edges) than those viewed face-on.

Our findings are of interest for the modeling and the interpretation of observations from a number of astrophysical sources:

Recently, an X-ray “Baldwin” effect was discovered by Iwasawa & Taniguchi (1993) in the Ginga data and with a much better statistics by Nandra et al. (1997b) in the ASCA data: The 6.4 keV Fe line and the reflection component in the Seyfert 1 X-ray spectra, which typically have  $2 - 10$  keV luminosities  $L_{2-10} \lesssim$  a few  $\times 10^{44}$  ergs  $s^{-1}$  can be well fit with reprocessing arising in low-ionization parameter material (Nandra et al. 1997a). Higher luminosity sources exhibit a *monotonic decrease* of the Fe line equivalent width (EW) (Nandra et al. 1997b). Above  $L_{2-10} \simeq 10^{45}$  ergs  $s^{-1}$ , the EW of the line drops abruptly and this line becomes undetectable for  $L_{2-10} \sim 10^{46}$  ergs  $s^{-1}$ , both in radio loud and radio quiet quasars. These observations are consistent with the general trend of our calculations which indicate that upon increase of the X-ray flux, *the X-ray reflecting material converts from “cold” to completely ionized*, with a concurrent decrease in the strength of the Fe 6.4 line, for the reasons discussed above. By contrast, models assuming a constant density for the illuminated gas predict that such an increase in the X-ray flux should give rise to the presence of intermediate states with even higher EW of He- and H-like iron lines and a deep broad iron edge (see Fig. 6, and also Fig. 1 in Matt

et al. 1993; Fabian 1998), which are not seen in the data. Our results show that, when computed self-consistently, i.e., using hydrostatic pressure balance, the line EW and the depth of the edge monotonically decrease in accordance with the observations. In future work we plan to explore in detail the interpretation of this effect in the context of general, global AGN models.

Another application of our code is the modeling of the reprocessing features in transient BH sources, because these cover a wide range of accretion rates  $10^{-4} < \dot{m} \leq 1$  while they decline from the maximum luminosity. In studying the X-ray reprocessing features and their relativistic smearing, one can potentially constrain such parameters of the accretion flow as the inner radius at which the disk terminates. This kind of modeling was in fact performed by Życki, Done & Smith (1997), who studied reprocessing features in GS 2023+338 during its decline Życki et al. (1998) who did the same for the Nova Muscae 1991 observations; and by Done & Życki (1999) for Cyg X-1. Given the results of this paper, it seems rather likely that the X-ray reprocessing calculations that include hydrostatic balance can make a noticeable difference in terms of how close to the black hole the “cold” matter is in these sources, and what is the evolution of the flow geometry during the luminosity decline.

Narrow Line Seyfert Galaxies (NLSG), that typically have steep X-ray spectra, may provide an additional opportunity to test accretion flows. As we found, steep X-ray spectra may lead to a sufficiently low Compton temperature, i.e.,  $kT_c \lesssim 1$  keV, which then allows some of the highest ionization stages of iron ion to be abundant enough to imprint “highly ionized” signatures on the X-ray spectra. In other words, due to steeper X-ray spectra, the hot Compton layer may now become visible (it is “invisible” for other objects with harder spectra because it does not produce any sharp line or absorption features), thus yielding interesting constraints on accretion flow geometry. Some of the observed NLSG indeed reveal unusual ionization states (see, e.g., Comastri et al. 1998 and Bautista & Titarchuk 1999).

## 8. CONCLUSIONS

In conclusion, we presented above a physically consistent way of computing the reprocessing features for any accretion disk geometry/model that does not produce X-ray driven winds. An important point to note is that the reflected spectra depend mostly on the gravity parameter  $A$ , which is determined by the illuminating flux, and the local gravity (or the ratio  $H/R$ ). The latter is independent of  $\alpha$ -parameter – the usual Shakura-Sunyaev viscosity parameter whose value is notoriously uncertain (see, e.g., Nayakshin, Rappaport & Melia 1999). Therefore, at least for a range of conditions (to be specified in a future paper), the resulting reprocessed X-ray spectra are independent of  $\alpha$  and thus can be unambiguously calculated for a given accretion disk model. Therefore, we believe that the methods presented in this paper may be used as a meaningful and sensitive test of theoretical predictions versus observations of the iron lines, edges and the reprocessing features in general. With advent of the new X-ray telescopes (Chandra, Astro-E and XMM), such tests may

bring us one step closer to establishing which (if any) of the current accretion disk models is correct.

SN acknowledges support by an NAS/NRC Associate-

ship during the course of this work. The authors thank Manuel Bautista, Chris Done, Julian Krolik, Daniel Proga, Lev Titarchuk and Piotr Życkifor many useful discussions.

## APPENDIX

### ON THE IMPORTANCE OF THERMAL HEAT CONDUCTION

We can estimate the maximum Thomson depth,  $\Delta\tau_m$ , of the region where the heat conduction is important by the following considerations. Suppose that  $\Delta z$  is the length scale over which the transition from the hot ( $T \sim 10^8$ ) solution to the cold one ( $T \sim 10^5$ ) occurs. The maximum heat flux due to conduction is the saturated conductive flux,

$$F_{\text{sat}} \sim c_h P, \quad (\text{A1})$$

where  $c_h$  is the isothermal sound speed at the hot (Compton) solution, and  $P$  is the gas pressure (see Cowie & McKee 1977, and also Max et al. 1980). The X-ray heating per unit volume can be estimated as  $Q_x^+ \sim n\sigma_x F_x$ , where  $\sigma_x$  is the total cross section, and  $n$  is the gas density. Therefore, heat conduction will dominate over distances no larger than  $\Delta z \lesssim F_{\text{sat}}/Q_x^+$ , yielding the corresponding maximum Thomson depth of

$$\Delta\tau_m = n\sigma_T \Delta z \sim \frac{F_{\text{sat}}}{Q_x^+} n\sigma_T \simeq \frac{Pc}{F_x} \frac{\sigma_T c_h}{\sigma_x c} \sim 10^{-3} T_8^{1/2}. \quad (\text{A2})$$

where  $T_8$  is the temperature of the hot zone adjacent to the temperature discontinuity in units of  $10^8$  K (note that  $\Delta z$  is essentially the ‘‘field length’’ introduced by Begelman & McKee (1990) when the conductive flux is given by the saturated flux). Here we made use of the fact that the transition from the hot to the cold solution happens when  $Pc/F_x \sim \text{few}^{-1}$ . Therefore, the direct influence of heat conduction on the radiation transfer is negligible because the Thomson depth of the region where conduction dominates is quite small (similar conclusions were obtained by KMT in their Appendix V). We in fact cannot afford to treat zones with such a small optical depth for numerical reasons, and thus taking thermal conduction into account is an expensive luxury for us. On the other hand, heat conduction may be quite important in determining what solution the system picks in the unstable regime, but we believe that we have taken its effects into account as discussed in §3.6.

### ON THE IMPORTANCE OF CLOUD FORMATION

In the case of a thermally unstable medium, the cold and hot phases may actually be mixed, i.e., the cold matter may be in the form of ‘‘clouds’’ embedded in the hot surrounding medium. Physics of cloud condensation and evaporation and radiative equilibria have been previously studied by, e.g., Zel’dovich & Pikel’ner 1969; Cowie & McKee 1977; KMT; Balbus 1985; Begelman & McKee and McKee & Begelman (1990). Although many aspects of the theory have been clarified in these papers, much uncertainty remains due to the unknown distribution of cloud sizes and separations. Rózańska & Czerny (1996), Rózańska (1999) studied the role of the thermal instability in X-ray illuminated disks in AGN. They argued that instead of a sharp transition from the hot to the cold solution, there exists a complex two-phase medium with cold clouds embedded in a hotter gas.

However, the gas density of the cold phase is much larger (by a factor of  $\sim 100 - 10^3$ ) than that of the hot medium, so the cold clouds experience a much greater gravitational force than the hot medium, and thus they will sink, joining the cold (one-phase) medium below. It seems quite likely that the gravity may separate the two phases, such that the hot phase will end up on the top of the cold phase just as a light oil does if poured into water, thus leading to a sharp boundary between the cold and the hot medium as suggested in our work here. In addition, note that a cloud can also be broken up if its ‘‘sinking velocity’’ is even a small fraction of the sound speed, since then the face-on pressure is larger than the pressure on the sides of the cloud. In addition, the incident X-ray flux may be variable, and thus can cause the height of the region where the two-phase medium may exist to be constantly changing, leading to cloud destruction before they can form. Finally, even if some clouds do form and are efficiently maintained in a part of the illuminated layer, we believe that their existence is marginal for the radiation transfer and the resulting spectra. Indeed, in the case of the quasar emission line regions, the clouds are thought to form above the accretion disk, in the region filled with a hot Compton-heated gas (e.g., Krolik et al. 1981). The latter, if optically thin, is basically invisible to the observer. Therefore, existence of any cool clouds embedded in this hot matter is of a significant observational interest, since the clouds are believed to be strong line emitters. In terms of a given spectral line, then, a cloud looks like a bright emitting object in the background of completely dark material.

The geometrical setup of the X-ray reprocessing problem is substantially different. The cool clouds, if formed, exist in the region *above* the cold thermally stable gas. Moreover, the temperature of the clouds should be close to the temperature of the cold stable phase below. This means that the emission spectrum of the clouds will be close to that of the cold material below. Thus, in terms of the observational signatures, except for increasing the amount of the cool material somewhat, the clouds will be completely washed out (unresolvable) on the background of the cold stable medium. Accordingly, we believe that existence of the two-phase medium in a region close to the temperature discontinuity is not only unclear, but is of academic value at least as far as the X-ray reprocessing is concerned.

## VISCIOUS DISSIPATION AND THE HYDROSTATIC EQUILIBRIUM

It has been pointed out to us by Julian Krolik that while the viscous dissipation can be neglected in the energy equation of the illuminated layer, one may still have to consider the effects of the viscous heating for hydrostatic balance (equation 19). This is so because the gravity is canceled mainly by the radiation pressure even in the illuminated layer of a radiation-dominated disk (see §5). Thus, there could be a situation in which the increase with height in the first term on the right in equations (19, 22) is entirely balanced by a corresponding increase in the outward radiation pressure force (the third term), which is exactly the case in a RD SS73 disk. One can show that for this to be true, the gas density of the illuminated layer must stay close to its midplane value (because viscous dissipation is usually modeled as being proportional to the gas density – see SS73), a rather unlikely condition for the illuminated matter in the setup of our paper. It is furthermore impossible if one resolves the vertical disk structure more accurately. Simulations (Agol and Krolik 1999, private communications) show that convection changes the disk profile in a way such that the gas density does not remain constant inside the RD disks; the gas density is greatest in the midplane and it decreases with height.

## REFERENCES

- Alme, M.L., & Wilson, J.R. 1974, *ApJ*, 194, 147.  
 Balbus, S.A. 1985, *ApJ*, 291, 518.  
 Basko, M.M., Sunyaev, R.A., & Titarchuk, L.G. 1974, *A&A*, 31, 249  
 Basko, M.M., Sunyaev, R.A., Hatchett, S., & McCray R. 1977, *ApJ*, 215, 276.  
 Bautista, M.A., & Titarchuk, L. 1999, *ApJ*, 511, 105.  
 Begelman, M.C., McKee, C.F., & Shields, G.A. 1983, *ApJ*, 271, 70.  
 Begelman, M.C., & McKee, C.F. 1990, *ApJ*, 358, 375.  
 Blackman, E.G. 1999, *MNRAS*, 306, L25.  
 Buff, J. & McCray, R. 1974, *ApJ*, 189, 147.  
 Comastri, A., et al. 1998, *A&A*, 331, 31  
 Cowie, L.L., & McKee, C.F. 1977, *ApJ*, 211, 135.  
 De Kool, M., & Wickramasinghe, D. T. 1999, *MNRAS*, in press  
 Done, C., & Życki, P.T., 1999, *MNRAS*, 305, 457.  
 Dove, J.B., Wilms, J., Maisak, M., & Begelman, M. 1997, *ApJ*, 487, 759.  
 Fabian, A.C. 1998, AIP Conference Proceedings 431., p.247  
 Field, G.B. 1965, *ApJ*, 142, 531.  
 Field, G.B., & Rogers, R.D. 1993, *ApJ*, 403, 94.  
 Galeev, A. A., Rosner, R., & Vaiana, G. S., 1979, *ApJ*, 229, 318.  
 George, I.M., & Fabian, A.C., 1991, *MNRAS*, 249, 352.  
 Guilbert, P., & Rees, M.J. 1988, *MNRAS*, 233, 475.  
 Haardt F., Maraschi, L., & Ghisellini, G. 1994, *ApJ*, 432, L95.  
 Iwasawa, K., & Taniguchi, Y., 1993, *ApJL*, 413, L15.  
 Kallman, T.R., & McCray, R. 1982, *ApJS*, 50, 263  
 Kallman, T.R., & Krolik, J.H., 1986, NASA/GSFC Laboratory for High Energy Astrophysics special report.  
 Ko, Y-K, & Kallman, T.R. 1994, *ApJ*, 431, 273.  
 Krolik, J.H., McKee, C.F., & Tarter, C.B. 1981, *ApJ*, 249, 422.  
 Krolik, J.H., Madau, P., & Życki, P.T. 1994, *ApJL*, 420, L57.  
 Liang, E.P., & Price, R.H. 1977, *ApJ*, 218, 247.  
 Lightman, A.P., & White, T.R. 1988, *ApJ*, 335, 57.  
 London, R., McCray, R., & Auer, L.H. 1981, *ApJ*, 243, 970.  
 Magdziarz, P., & Zdziarski, A.A. 1995, *MNRAS*, 273, 837.  
 Matt, G., Fabian, A.C., Ross, R.R. 1993, *MNRAS*, 262, 179.  
 Max, C.E., McKee, C.F., & Mead, W.C. 1980, *Phys. Fluids*, 23, 1620  
 McCray, R., & Hatchett, S. 1975, *ApJ*, 199, 196.  
 McKee, C.F., & Begelman, M.C. 1990, *ApJ*, 358, 392.  
 Mihalas, D. 1978, *Stellar Atmospheres*, W.H. Freeman and Company, San Francisco  
 Nandra, K. et al. 1997a, *ApJ*, 477, 602.  
 Nandra, K. et al. 1997b, *ApJL*, 488, L9.  
 Nayakshin, S., & Melia, F. 1997a, *ApJL*, 484, L103.  
 Nayakshin, S., & Melia, F. 1997b, *ApJL*, 490, L13.  
 Nayakshin, S., & Melia, F. 1997c, unpublished, astro-ph/9709286  
 Nayakshin, S. 1998a, in “Quasars and Cosmology”, ASP Conference Series, ed. G. Ferland & J. Baldwin, p. 43; astro-ph/9812109  
 Nayakshin, S. 1998b, in “Quasars and Cosmology”, ASP Conference Series, ed. G. Ferland & J. Baldwin, p. 87; astro-ph/9812108  
 Nayakshin S. 1998c, PhD thesis, University of Arizona (astro-ph 9811061).  
 Nayakshin S., & Dove, J.B. 1999, submitted to *ApJ* (astro-ph 9811059).  
 Nayakshin, S., Rappaport, S., & Melia, F. 1999, submitted to *ApJ*, astro-ph/9905371  
 Poutanen, J., Nagendra, K.N., & Svensson, R. 1996, *MNRAS*, 283, 892.  
 Proga, D. 1999, *MNRAS*, 304, 938.  
 Proga, D., Stone, J.M., & Drew, J.E. 1998, *MNRAS*, 295, 595.  
 Raymond, J.C. 1993, *ApJ*, 412, 267.  
 Reynolds, C.S., & Begelman, M.C. 1997, *ApJ*, 488, 109.  
 Rózańska, A., & Czerny, P.T. 1996, *Acta Astron.*, 46, 233  
 Rózańska, A., 1999, submitted to *MNRAS*, astro-h/9807227  
 Rózańska, A., Czerny, B., Życki, P.T., & Pojmanski, G. 1999, *MNRAS*, 305, 481.  
 Ross, R.R., & Fabian, A.C. 1993, *MNRAS*, 261, 74.  
 Ross, R.R., Fabian, A.C., & Brandt, W.N. 1996, *MNRAS*, 278, 1082.  
 Ross, R.R., Fabian, A.C., & Young, A.J. 1999, *MNRAS*, 306, 461.  
 Shakura, N.I., & Sunyaev, R.A. 1973, *A&A*, 24, 337  
 Sincell, M.W., & Krolik, J.H. 1997, *ApJ*, 476, 605.  
 Svensson, R. & Zdziarski, A. A. 1994, *ApJ*, 436, 599.  
 Svensson, R. 1996, *A&AS*, 120, 475  
 White, T.R., Lightman, A.P., & Zdziarski, A.A. 1988, *ApJ*, 331, 939.  
 Zel’dovich, Y.B., & Pikel’ner, S.B. 1969, *Soviet Phys. – JETP*, 29, 170  
 Życki, P.T., Krolik, J.H., Zdziarski, A.A., & Kallman, T.R. 1994, *ApJ*, 437, 597.  
 Życki, P.T., Done, C., & Smith, D.A. 1997, *ApJL*, 488, L113.  
 Życki, P.T., Done, C., & Smith, D.A. 1998, *ApJL*, 496, L25.

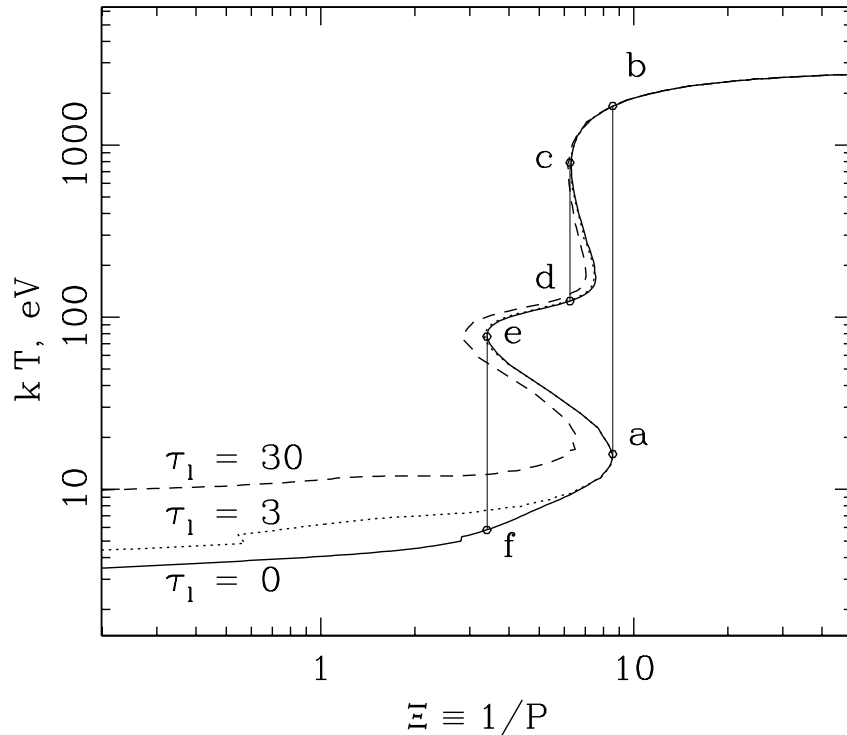


Fig. 1.— Several illustrative ionization equilibrium curves (“S-curves”) showing dependence of the gas temperature,  $T$ , on the ionization parameter  $\Xi$  for three different values of the optical depth in resonance lines. See text for discussion.

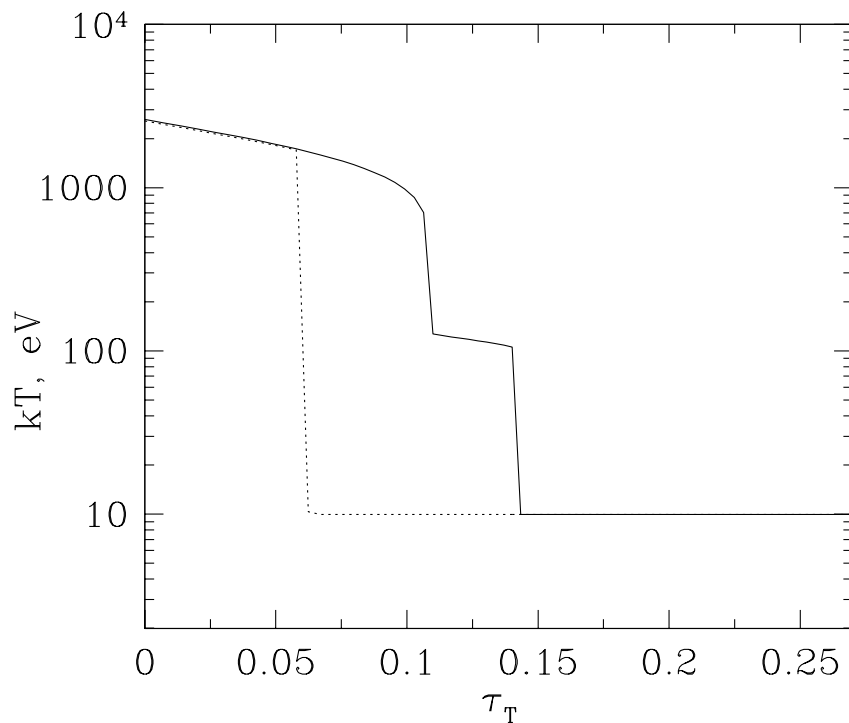


Fig. 2.— Temperature of the illuminated layer as a function of the Thomson depth when all the lines are assumed to be optically thin. The solid curve is calculated with a high initial temperature guess ( $kT_{in} = 3$  keV), whereas the dotted curve shows results of a simulation with a low initial temperature guess ( $kT_{in} = 10$  eV). Note that all other parameters in these two cases are equal, so that the different outcomes illustrate the uncertainty that exists due to multiple solutions allowed in the thermally unstable region.

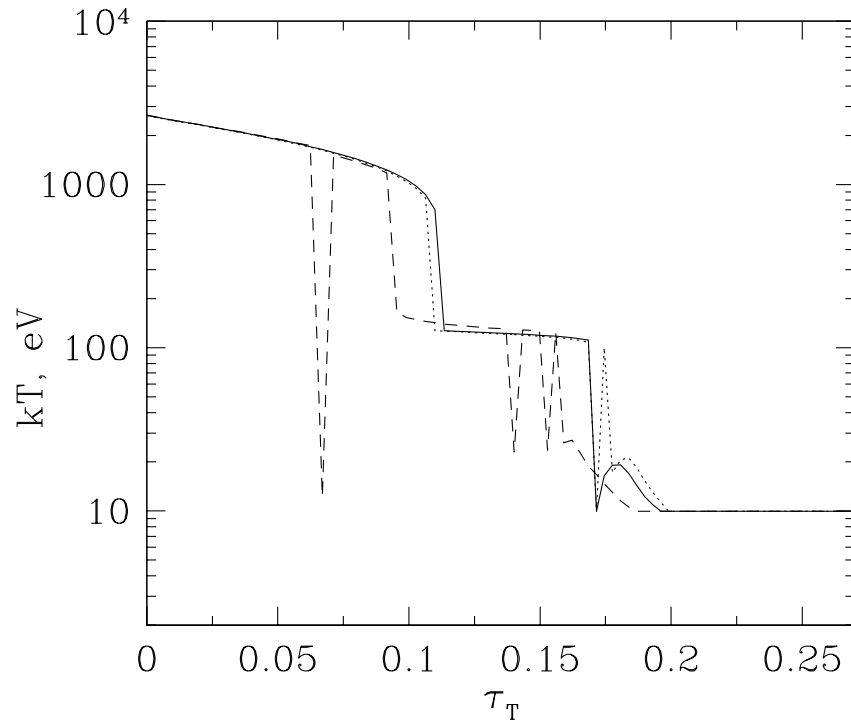


Fig. 3.— Temperature of the illuminated layer as a function of the Thomson depth when the line depths are calculated self-consistently. The dotted curve is for solution found by providing XSTAR with a high initial temperature guess for each zone ( $kT_{in} = 3 \text{ keV}$ ); the dashed curve is for the simulation with a low initial temperature guess ( $kT_{in} = 10 \text{ eV}$ ), and the solid curve is computed with  $T_{in} = 1.5 \times T_{prev}$ , where  $T_{prev}$  is the temperature of the previous zone.

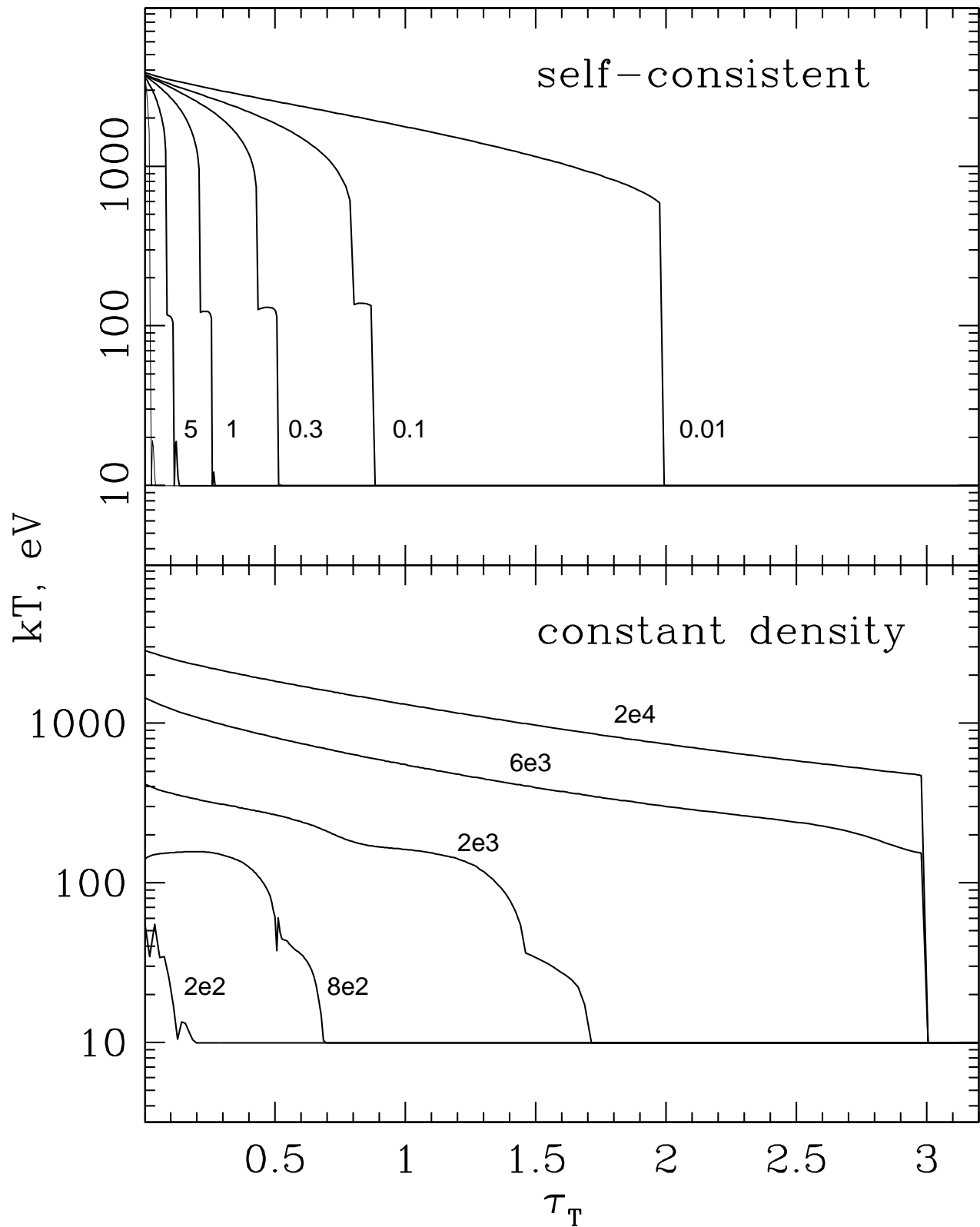


Fig. 4.— *Lower Panel:* Temperature of the illuminated gas atmosphere as a function of the Thomson optical depth computed with the constant density assumption. The parameter values are  $F_x = 10^{16}$  erg cm $^{-2}$  s $^{-1}$  and  $\Gamma = 1.9$  for all the tests. The value of the density ionization parameter  $\xi$  is shown next to the corresponding curve. *Upper Panel:* Temperature of the illuminated gas atmosphere computed with our self-consistent approach. The curves differ by their respective values of the gravity parameter  $A$ , whose value is shown to the right of the corresponding curve ( $A = 20$  for the fine solid curve). Note that the self-consistent solution “avoids” the unstable regions of the S-curve, whereas the constant density solutions unphysically cover the whole temperature range between the effective and the Compton temperature.

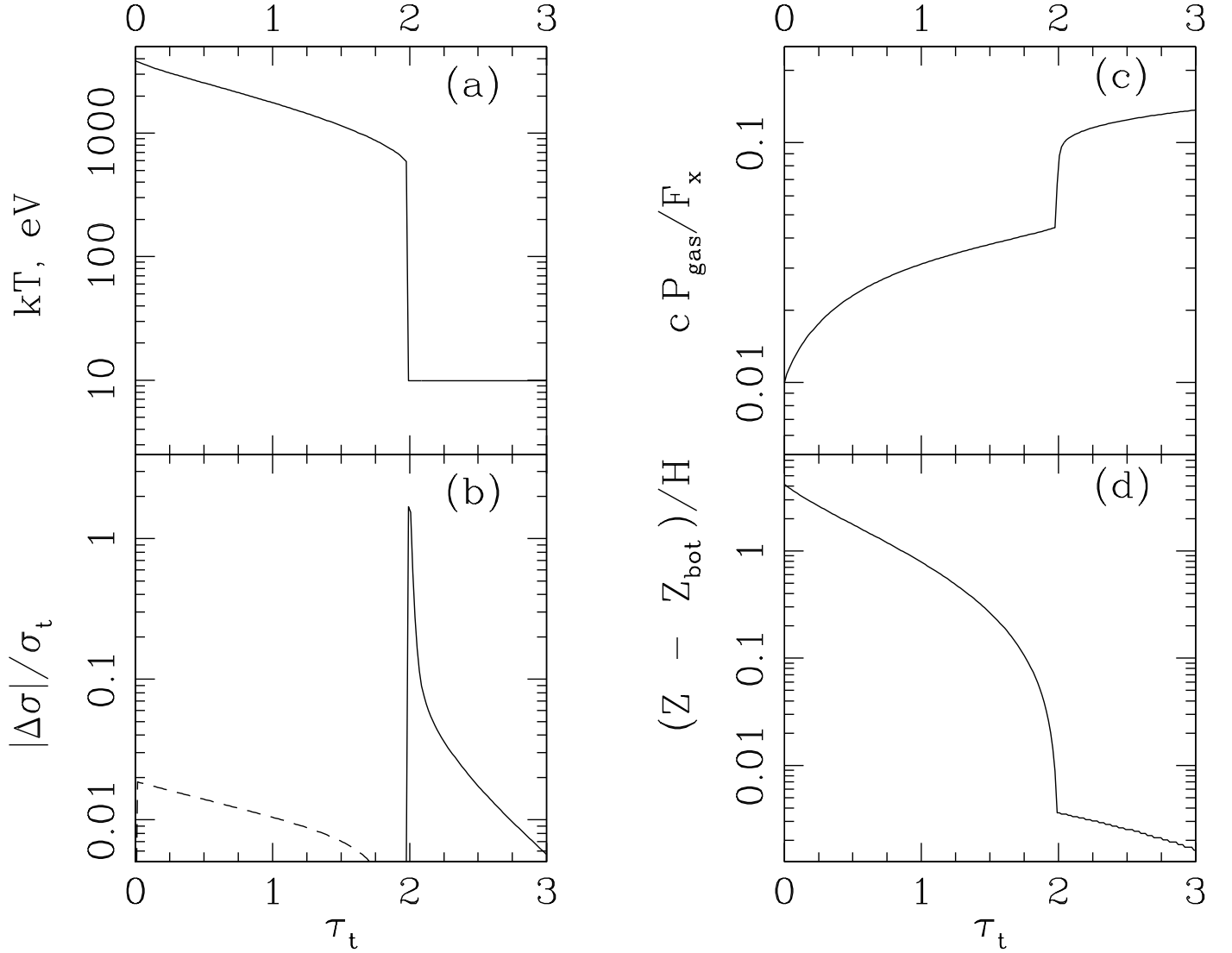


Fig. 5.— (a) Gas temperature, (b) radiation pressure force multiplier (see eq. 22), (c) the gas pressure, and (d) the height above the bottom of the layer ( $z_b$ ) for the model with  $A = 0.01$ . In panel (b), positive values of  $\Delta\sigma$  are depicted with a dashed curve, whereas negative values are shown by the solid curve. Note that the positive sign of  $\Delta\sigma$  in the Compton-heated layer is due to the relativistic roll-over in the Klein-Nishina cross section for the incident hard X-rays.

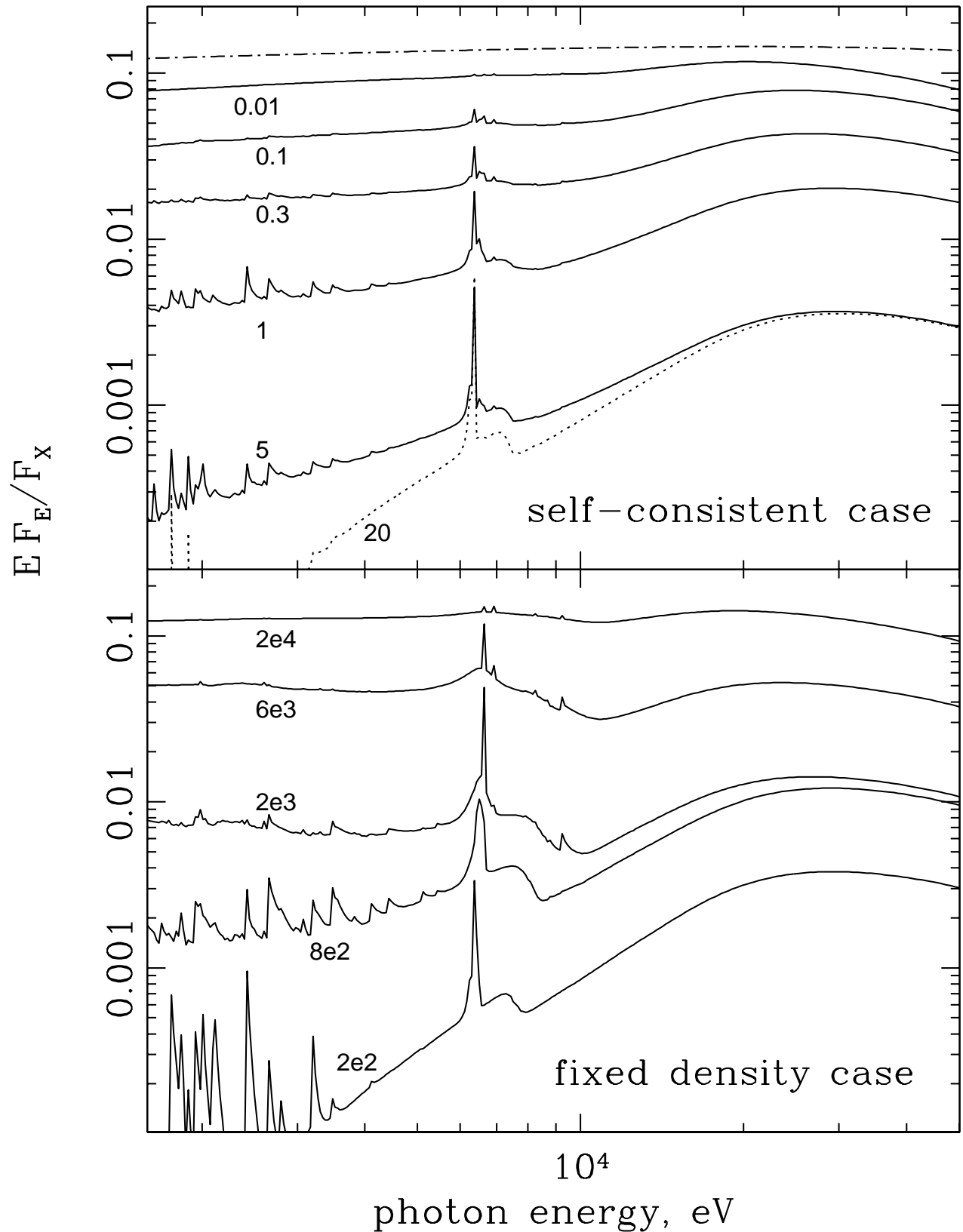


Fig. 6.— Reflected spectra for the tests presented in Fig. (4). The incident ionizing spectrum is shown with the dash-dotted curve. The curves are shifted by arbitrary factors for clarity. Parameter values are printed next to their respective curves. Note that evolution of the reprocessing features in the constant density cases (*lower panel*) is distinctly different from that for the self-consistent calculations (*upper panel*).

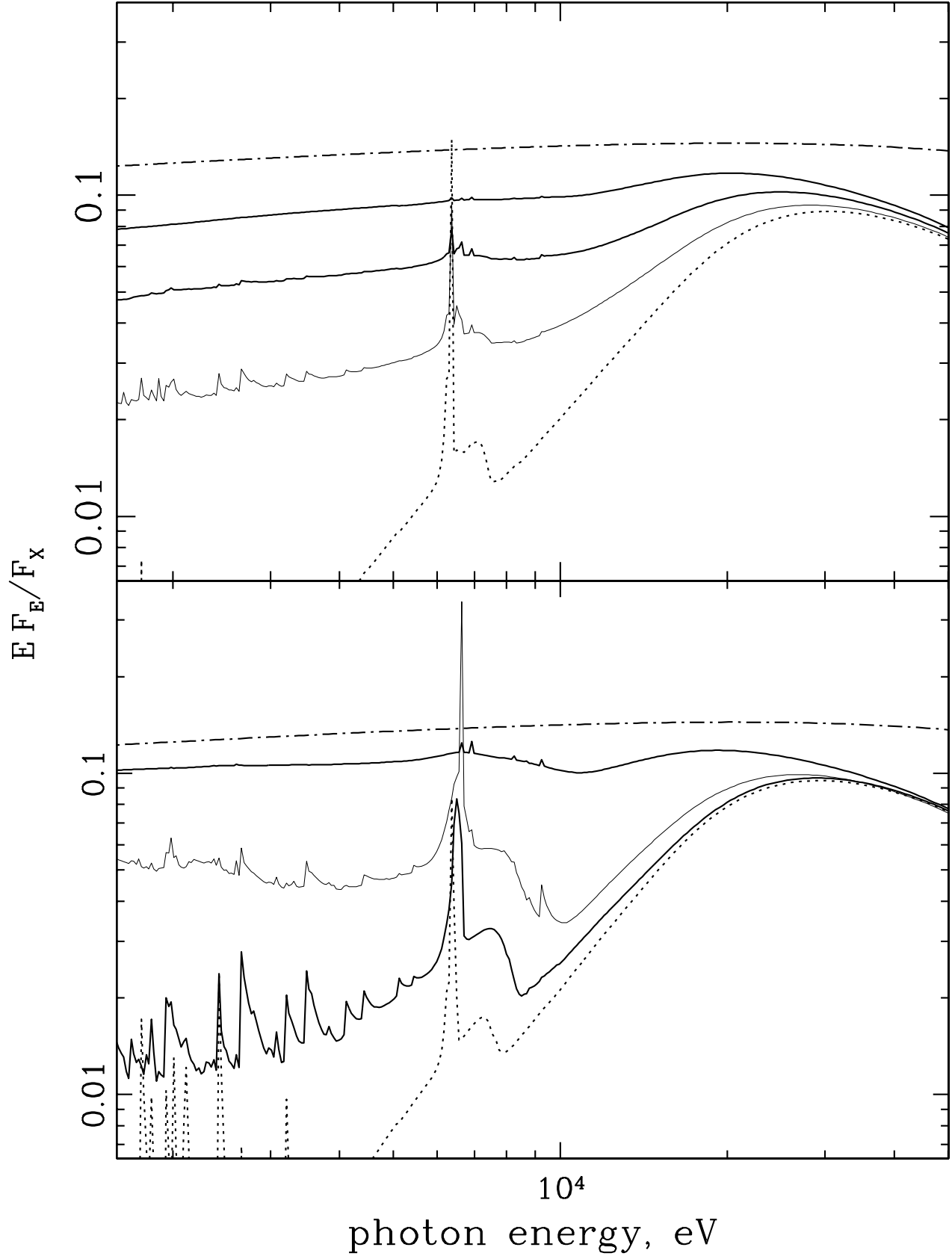


Fig. 7.— Selected curves from Fig. (6) plotted with the correct normalization. The incident ionizing spectrum is shown with the dash-dotted curve. The parameter values for the curves are:  $A = 20, 1, 0.1, 0.01$  bottom to top for the *upper panel*, and  $\xi = 200, 800, 2 \times 10^3$  and  $2 \times 10^4$  bottom to top for the *lower panel*.

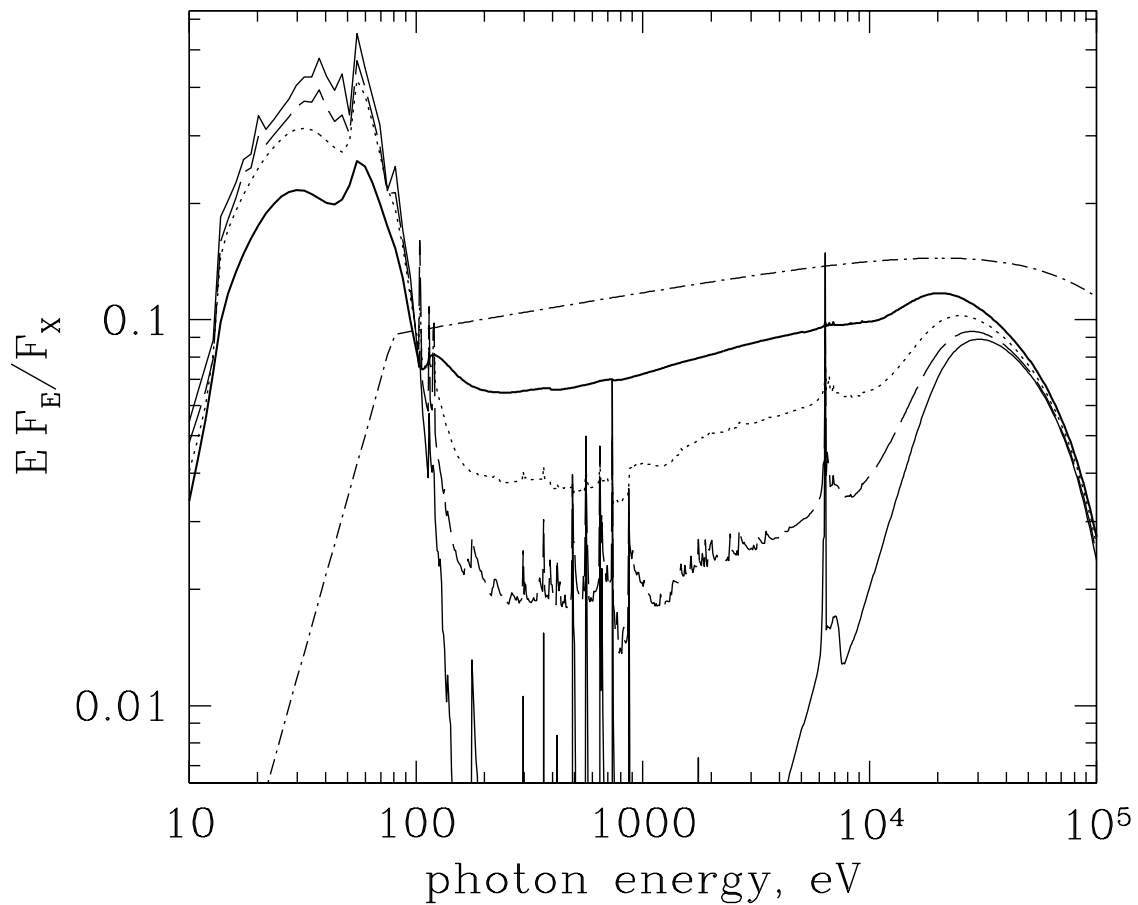


Fig. 8.— The angle-averaged reflection spectra for the tests shown in the upper panel of Fig. 6. Note that the main effect of the Comptonized layer is to fill in the gap (caused by photoabsorption in the interval from  $\sim 100$  eV to  $\sim 10$  keV) between the thermalized part of the reflected spectrum and the X-ray reflection component.

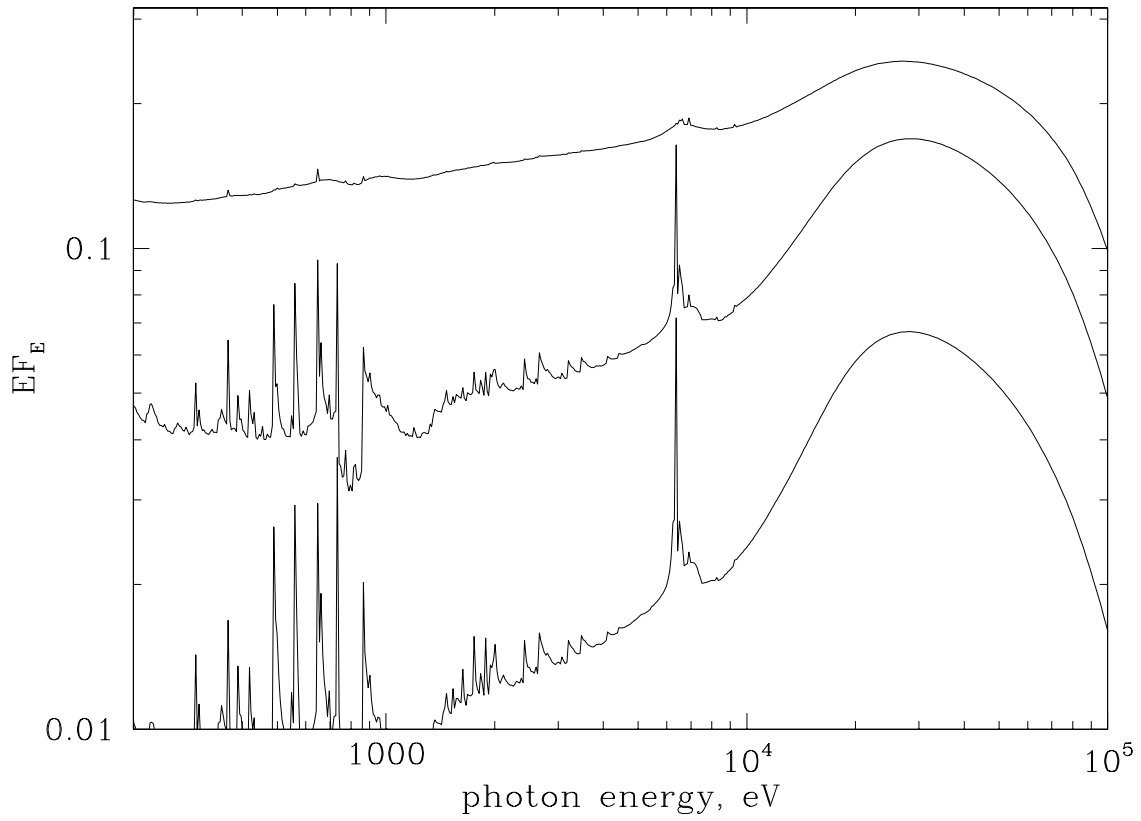


Fig. 9.— Reflected spectra (intensities) at different viewing angles  $i$  with respect to the normal to the disk for the self-consistent case with  $A = 1$  shown in Figs. 4 & 6. The cosines of the angles are  $\mu \equiv \cos i = 1/16$ ,  $7/16$  and  $15/16$  for upper, middle and the bottom curves, respectively. For clarity of presentation, the middle curve is scaled down by 1.2, whereas the bottom curve rescaled by 2.5.

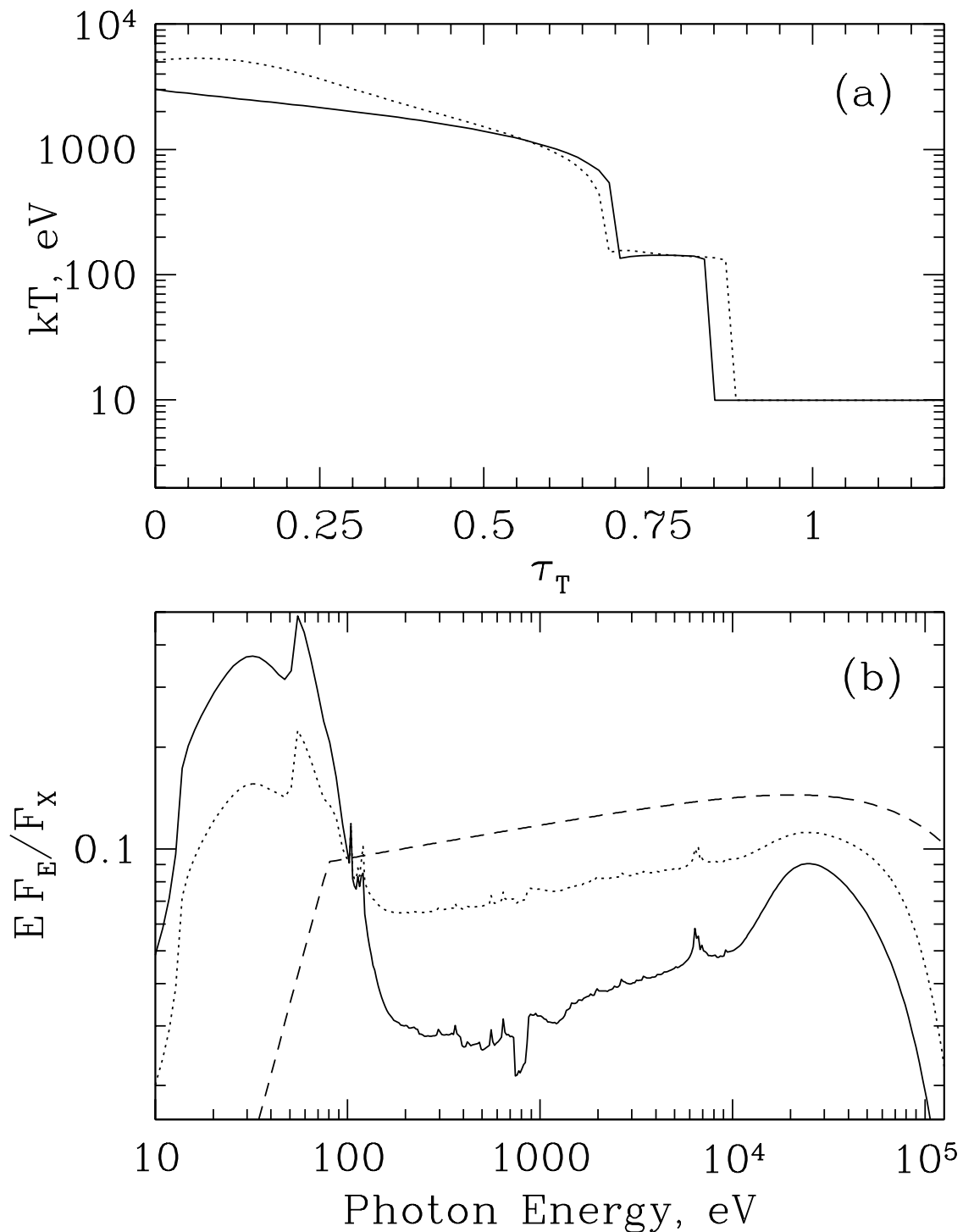


Fig. 10.— *Upper panel:* Temperature profile for the self-consistent calculations with  $A = 0.1$  for different angles of the X-ray incidence with respect to the normal to the disk. The cosines of the angles are  $15/16$ , and  $1/16$  for the solid and dotted curves, respectively. *Lower Panel:* Angle-averaged reflected spectra for the two tests shown in the upper panel, together with the ionizing spectrum depicted by the dashed curve.

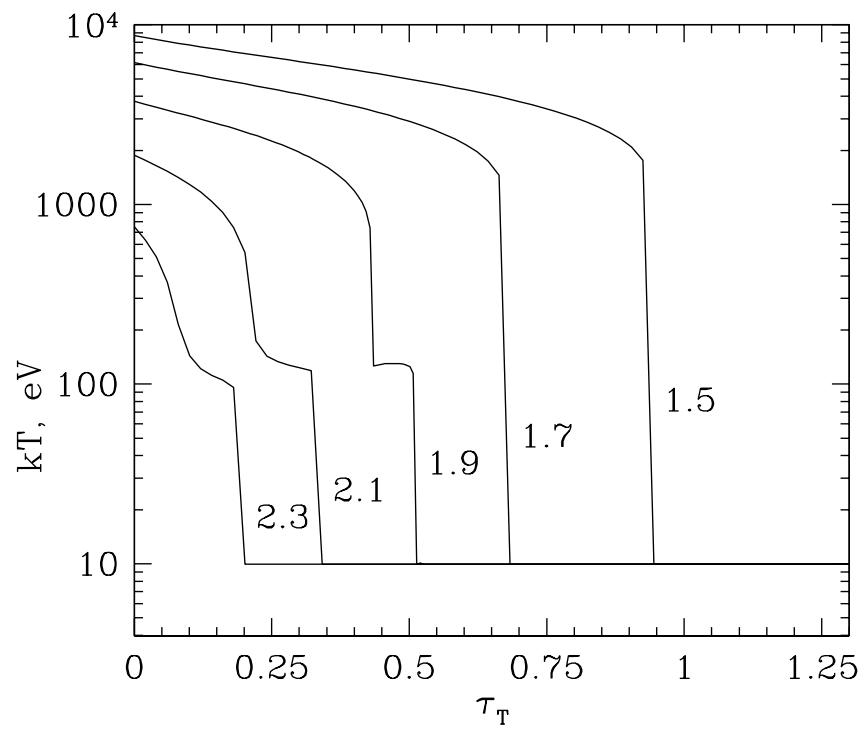


Fig. 11.— Temperature profile for self-consistently computed tests with  $A = 0.3$ ,  $F_x = 10^{16}$  erg cm $^{-2}$  s $^{-1}$  and isotropic illuminating flux for five different values of the spectral index  $\Gamma$  of the ionizing radiation. Values of  $\Gamma$  are shown to the right of the respective curve.

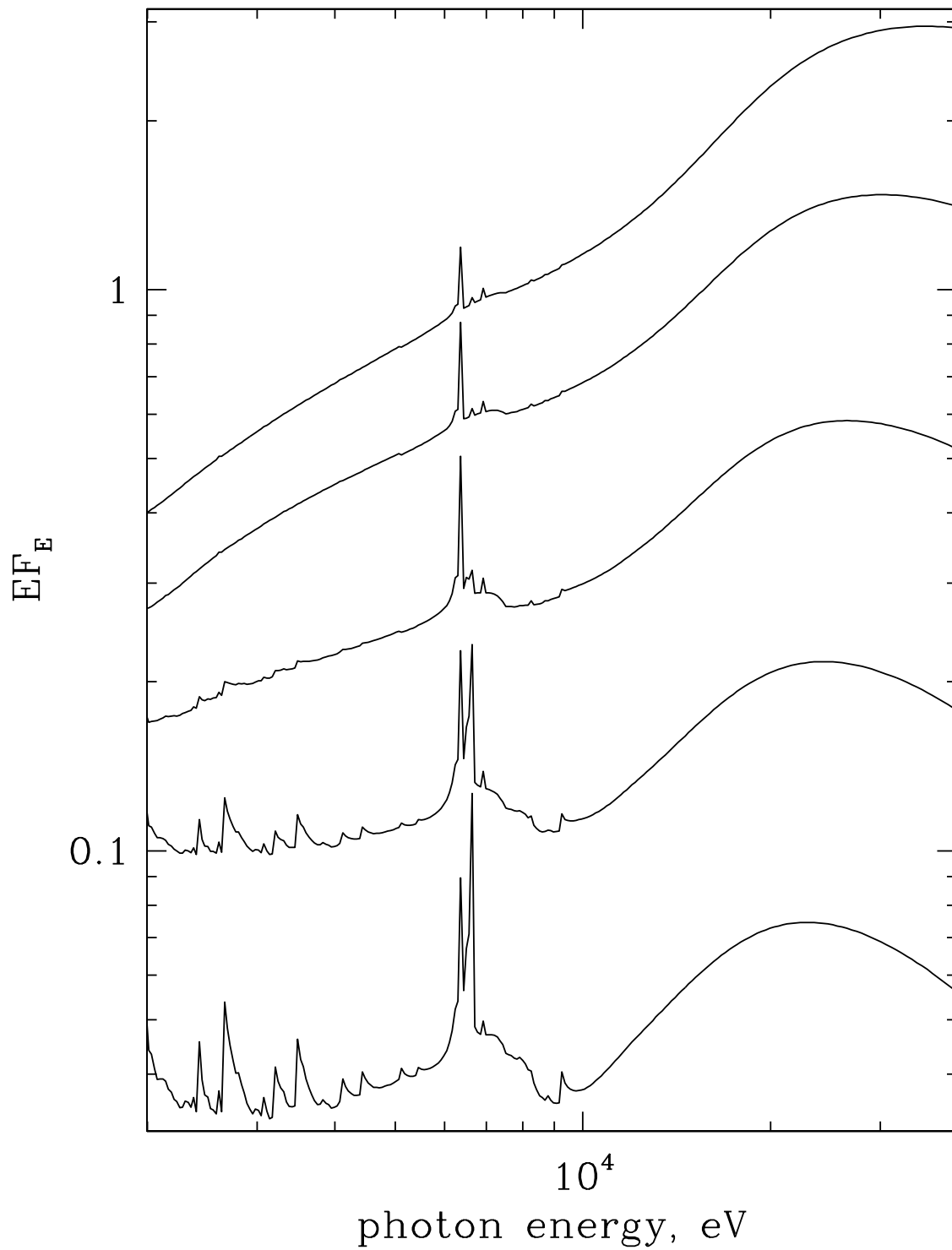


Fig. 12.— Reflected spectra for five different values of  $\Gamma$  for the tests presented in Fig. (11). The upper curve corresponds to  $\Gamma = 1.5$  and the lower one to  $\Gamma = 2.3$ . Curves are shifted with respect to one another to allow an easy comparison.

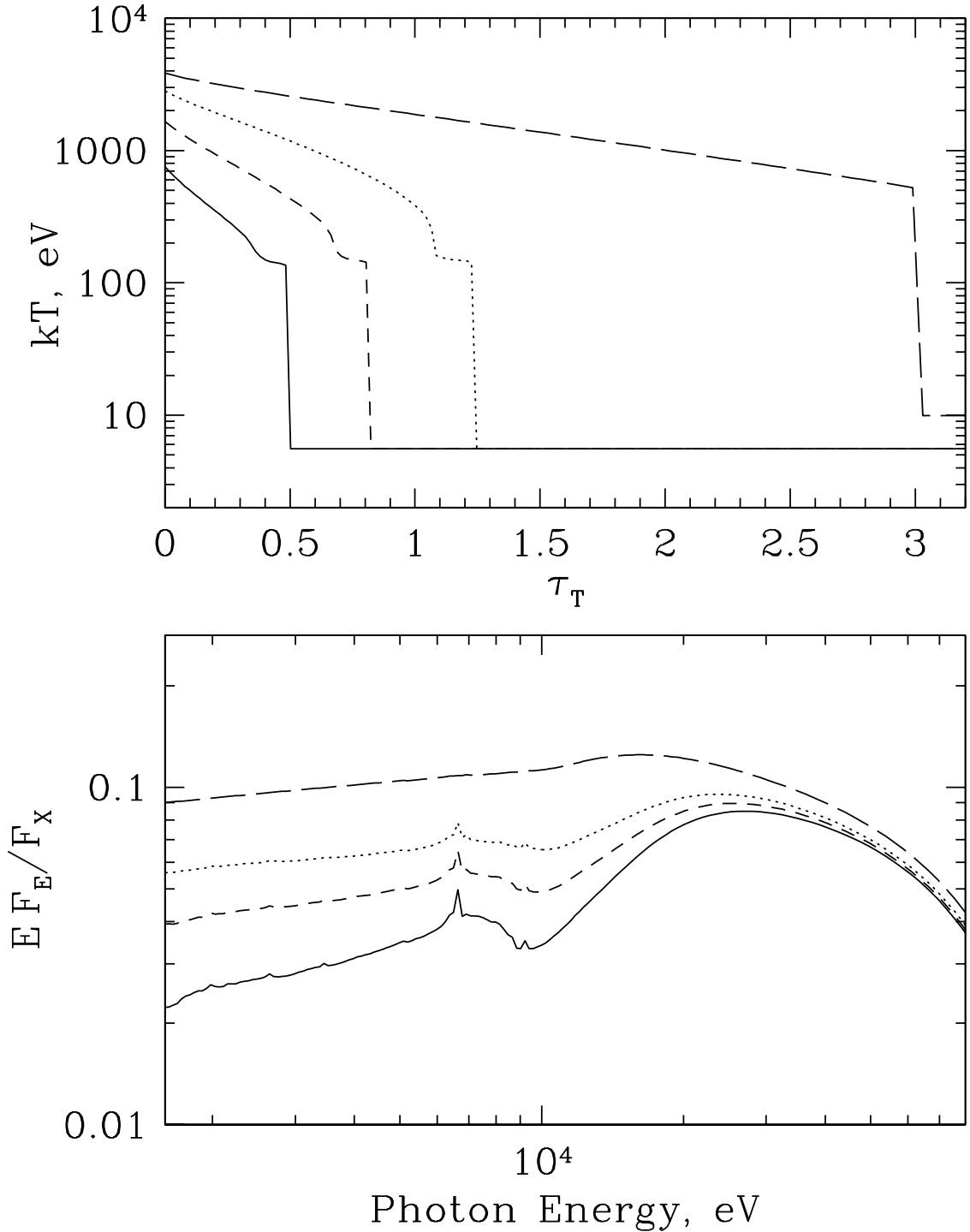


Fig. 13.— Temperature profiles (upper panel) and reflected spectra (lower panel) for a radiation dominated disk accreting at  $\dot{m} = 0.1$  and  $M_8 = 1$ . The  $A$ -parameter is self-consistently found for a given incident X-ray flux, which is equal to  $10^{16}$  erg cm $^{-2}$  s $^{-1}$  for the long-dashed curve, and  $10^{15}$  erg cm $^{-2}$  s $^{-1}$  for the rest of the curves. The dotted curve is computed for the self-consistent value of the disk intrinsic flux  $F_d$  (i.e.,  $F_d/F_x = 0.63$  for this case), whereas it is 4 and 12 times this value for the short-dashed and solid curves, respectively.